

On the merits of sparse surrogates for global sensitivity analysis of multi-scale nonlinear problems: application to turbulence and fire-spotting model in wildland fire simulators

A. Trucchia^a, V. Egorova^a, G. Pagnini^{a,b}, M.C. Rochoux^c

^a*BCAM – Basque Center for Applied Mathematics, Alameda de Mazarredo 14, 48009 Bilbao, Basque Country – Spain*

^b*Ikerbasque – Basque Foundation for Science, Calle de María Díaz de Haro 3, 48013 Bilbao, Basque Country – Spain*

^c*CECI, Université de Toulouse, CNRS, CERFACS, 42 Avenue Gaspard Coriolis, 31057 Toulouse cedex 1, France*

Abstract

Many nonlinear phenomena, whose numerical simulation is not straightforward, depend on a set of parameters in a way which is not easy to predict beforehand. Wildland fires in presence of strong winds fall into this category, also due to the occurrence of firespotting. We present a global sensitivity analysis of a new sub-model for turbulence and fire-spotting included in a wildfire spread model based on a stochastic representation of the fireline. To limit the number of model evaluations, fast surrogate models based on generalized Polynomial Chaos (gPC) and Gaussian Process are used to identify the key parameters affecting topology and size of burnt area. This study investigates the application of these surrogates to compute Sobol' sensitivity indices in an idealized test case. The performances of the surrogates for varying size and type of training sets as well as for varying parameterization and choice of algorithms have been compared. In particular, different types

of truncation and projection strategies are tested for gPC surrogates. The best performance was achieved using a gPC strategy based on a sparse least-angle regression (LAR) and a low-discrepancy Halton's sequence. Still, the LAR-based gPC surrogate tends to filter out the information coming from parameters with large length-scale, which is not the case of the cleaning-based gPC surrogate. The wind is known to drive the fire propagation. The results show that it is a more general leading factor that governs the generation of secondary fires. Using a sparse surrogate is thus a promising strategy to analyze new models and its dependency on input parameters in wildfire applications.

Keywords: Sensitivity Analysis, generalized Polynomial Chaos, Gaussian Process, Wildland fire

¹ Nomenclature

Table 1: List of abbreviations

Abbreviation	Meaning
ABL	Atmospheric Boundary Layer
FT	Free Atmosphere
GP	Gaussian Process
gPC	generalized Polynomial Chaos
LAR	Least Angle Regression
LSM	Level Set Method
MSR	Minimum Spanning Rectangle
PDF	Probability Density Function
ROS	Rate of Spread
SLS	Standard Least Squares
STD	STandard Deviation

Table 2: List of important static and dynamic model parameters.

Model quantities	Units
$\mathcal{B}(t)$, burnt area at time t	—
f , PDF of the random process	m^{-2}
$G(\mathbf{x}; t)$, isotropic bivariate Gaussian PDF of turbulence	m^{-2}
$q(l)$, lognormal PDF of firebrand landing distance	m^{-1}
$\mathbf{x} = (x_1, x_2)$, horizontal space variable	m
\mathbf{n}_{fr} , normal direction to the fireline	—
\mathbf{n}_{U} , unit vector aligned with the mean wind direction	—
t , time	s
ϕ , level-set function	—
Ω , 2-D computational domain	—
$ \Omega $, area of the computational domain	m^2
Physical Model Parameters	Value/Units
C_d , drag coefficient	—
D , turbulent diffusion coefficient	$\text{m}^2 \text{s}^{-1}$
g , acceleration due to gravity	9.8 m s^{-2}
h , dimension of convective cell	100 m
H , fire plume height	m
I , fireline intensity	kW m^{-1}
P_{f0} , reference fire power	10^6 W
\mathbf{U} , horizontal wind vector field at mid-flame height	m s^{-1}
$\ \mathbf{U}\ $, horizontal wind magnitude	m s^{-1}
\mathcal{V} , rate of spread	m s^{-1}
z_p , p th percentile	0.45
Δh_c , heat of combustion of wildland fuels	$18,620 \text{ kJ kg}^{-1}$
(μ, σ) , parameters of the log-normal PDF $q(l)$	—
ρ_a , air density	1.2 kg m^{-3}
ρ_f^* , wildland fuel density (<i>Pinus Ponderosa</i>)	542 kg m^{-3}
ω_0 , oven-dry mass of wildland fuel	2.243 kg m^{-2}
τ , ignition delay of firebrands	s
χ , air thermal diffusivity	$2 \cdot 10^{-5} \text{ m}^2 \text{s}^{-1}$
ΔT , temperature difference of convective cell	$800\text{-}923 \text{ K}$
ℓ , firebrand landing distance	m
ν , kinematic viscosity	$1.5 \cdot 10^{-5} \text{ m}^2 \text{s}^{-1}$
γ , thermal expansion coefficient	K^{-1}
$\alpha_H, \beta_H, \gamma_H, \delta_H$, coefficients for fire plume height H	—

Table 3: List of important algorithmic parameters.

A_t ,	burnt area ratio at time t
d ,	dimension of the stochastic space ($d = 3$)
\mathcal{D}_N ,	training set of size N
\mathcal{M} ,	forward model
\mathcal{M}_{pc} ,	gPC-expansion
N ,	size of the training set
P ,	total polynomial order
q ,	hyperbolic truncation parameter
r ,	number of terms in the surrogate basis
S_t ,	minimum spanning rectangle ratio at time t
y ,	quantity of interest
\hat{y} ,	estimate of the quantity of interest y
$y^{(k)}$,	k th realization of the quantity of interest y
\mathcal{A} ,	set of selected multi-indices in gPC-expansion
α ,	multi-index for gPC-expansion
δ ,	Kronecker delta-function
$\boldsymbol{\theta} = (\theta_1, \dots, \theta_d)$,	vector of uncertain input parameters, $[\ \mathbf{U}\ , I, \tau]$ or $[\mu, \sigma, D]$
$\boldsymbol{\theta}^{(k)}$,	k th realization of the uncertain input vector $\boldsymbol{\theta}$
$\boldsymbol{\zeta} = (\zeta_1, \dots, \zeta_d)$,	vector $\boldsymbol{\theta}$ in standard probabilistic space
ρ_{θ_i} ,	marginal PDF of i th input parameter in $\boldsymbol{\theta}$
$\rho_{\boldsymbol{\zeta}}$,	joint PDF of $\boldsymbol{\theta}$ in standard probabilistic space
Ψ_{α} ,	α th basis function for surrogate model
Φ_{α_i} ,	i th one-dimensional basis function
γ_{α} ,	α th coefficient in the surrogate basis
$\boldsymbol{\gamma}$,	vector of surrogate coefficients
$(\omega^{(k)}, \boldsymbol{\zeta}^{(k)})$,	k th quadrature weight and root
ℓ_{gp} ,	correlation length-scale for GP-model
σ_{gp} ,	observable standard deviation for GP-model
τ_{gp} ,	nugget effect for GP-model
$\pi(\boldsymbol{\theta}, \boldsymbol{\theta}')$,	correlation kernel for GP-model
ϵ_{emp} ,	empirical training error
Q_2 ,	cross-validation predictive coefficient

2 1. Introduction

3 Despite our recent progress in computer-based wildland fire spread mod-
4 eling and remote sensing technology, our general understanding of wildland
5 fire behavior remains limited. This is mainly due to the complexity of wild-
6 fire dynamics that results from multi-scale interactions between biomass py-
7 rolysis, combustion and turbulent flow dynamics, heat transfer as well as
8 atmospheric dynamics [1, 2, 3, 4, 5, 6]. Turbulence plays an important role:
9 wildland fires release large amounts of heat that lead to the development
10 of a turbulent flow in the vicinity of the flame zone and thereby enhance
11 the heat transfer to unburnt fuel, boosting biomass fuel ignition, combustion
12 and fire spread. There is therefore a strong coupling between wildland fires
13 and micrometeorology [7, 8, 9, 10, 11, 12]. When extreme conditions are
14 met in complex terrain such as canyons in combination with strong winds
15 and severe drought, highly destructive fires referred to as “megafires” can
16 develop [13, 14, 15, 16]. For such fires, a massive buoyant smoke plume
17 forms above the flame zone modifying micro-meteorological conditions [17]
18 and thereby fire spread conditions. Windborne embers can be transported
19 over large distances, causing fire spotting and further ignitions downstream
20 from the current fire, leading to multiple “spot fires” that are difficult to
21 stop by firefighters and that dramatically increase fire danger. Turbulence
22 and fire-spotting result from very nonlinear effects that are still poorly un-
23 derstood and that have been identified as a valuable research target with
24 direct applications in fire emergency response, especially at wildland-urban
25 interface [18].

26 The representation of these processes is beyond the scope of current oper-

27 ational wildfire spread models. At regional scales (i.e. at scales ranging from a
 28 few tens of meters up to several hectares), a wildland fire is indeed represented
 29 as a two-dimensional propagating interface (referred to as the “fire front” or
 30 “fireline”) separating the burnt area to the unburnt vegetation; the local
 31 propagation speed is called the “rate of spread” (ROS). This front represen-
 32 tation is the dominant approach in current wildfire spread simulators such as
 33 FARSITE [19], FOREFIRE [20, 12], PROMETHEUS [21], PHOENIX Rapid-
 34 Fire [22], SFIRE [11] or ELMFIRE [23]. These simulators rely on an empiri-
 35 cal parametrization of the ROS that is derived from steady-state assumption
 36 and that is an analytic function of biomass fuel properties, topographical
 37 properties and micro-meteorological conditions [24]. The ROS submodel is
 38 included in an Eulerian or Lagrangian front-tracking solver to simulate the
 39 fireline propagation. This approach is limited in scope [25, 26, 27] due to
 40 the large uncertainties associated with the input parameters of the ROS
 41 model [28, 29], which can be partially reduced by integrating real-time fire
 42 front measurements through data assimilation [11, 30, 31, 32, 33, 34, 35, 36].
 43 This approach is also limited due to the lack of knowledge on the physics of
 44 the fire problem [5], in particular on the processes associated with turbulence
 45 and fire-spotting.

46 These modeling limitations at regional scales have motivated investiga-
 47 tion of turbulence and fire-spotting effects both from experimental and mod-
 48 eling viewpoints [37, 38, 39, 40, 18, 41, 42, 43, 44]. To better characterize
 49 these nonlinear processes, there is a need to develop new submodels includ-
 50 ing the effects of random processes such as turbulence and fire-spotting in
 51 operationally-oriented wildfire spread models. This is one of the objectives of

52 the work proposed in [45, 46, 47, 48], which introduces a randomized repre-
 53 sentation of the fireline. A novel family of reaction-diffusion equations have
 54 been developed to link front models to reaction-diffusion ones and thereby
 55 integrate the effects of random processes in fire models. The front propaga-
 56 tion is randomized by adding to the driving function, a random displacement
 57 distributed according to a probability density function (PDF) corresponding
 58 to heat turbulent transport and fire-spotting landing distance. The driving
 59 equation of the resulting averaged process is analogous to an evolution equa-
 60 tion of the reaction-diffusion type, where the ROS controls the source term.
 61 In absence of random processes, the model is identical to the one given by
 62 the standard wildfire spread model, which is only driven by the ROS analytic
 63 function.

64 Including new modeling components in wildfire spread simulators adds
 65 some complexity and in particular introduces new model parameters. There
 66 is therefore a strong need to perform sensitivity analysis to analyze in a
 67 rigorous way the model structure, i.e. the dependency between the input pa-
 68 rameters and the simulated quantities of interest (here, the topology and the
 69 extension of the burnt area at a given time). The objective in such an exten-
 70 sive global sensitivity analysis is two-fold. First, sensitivity analysis identifies
 71 the most influential parameters on the model predictions over a wide range
 72 of values for the model parameters, ranks them by order of importance and
 73 spots unimportant parameters [49, 50, 51]. This is helpful to provide hints
 74 and guidelines about the physical processes that are essential to account for
 75 to track wildland fire behavior. Second, sensitivity analysis is a mandatory
 76 step to select which are the estimation targets to consider when the wild-

77 fire spread model is integrated in a data assimilation framework to produce
78 short-term predictions of wildfire behavior; the model parameters shall in-
79 deed be uncertain and the quantities of interest shall be sensitive to changes
80 in these model parameters to ensure data assimilation is efficient [52, 32, 35].

81 When relying on stochastic non-intrusive methods (meaning that no mod-
82 ification of the physical model, also referred to as the “forward model”, is
83 required), global sensitivity analysis requires the use of an ensemble of model
84 evaluations. This procedure can be divided into three steps: *i*) characteriza-
85 tion of the variability in the model parameters based on available information
86 and statistical sampling to obtain an ensemble of parameter values; *ii*) mul-
87 tiple evaluations of the forward model while accounting for the identified un-
88 certainties to obtain an ensemble of quantities of interest (the forward model
89 is used as a “black-box”); and *iii*) computing Sobol’ sensitivity indices [53]
90 that provides a relative measure of how the variability of the model response
91 is affected by the variability in each uncertain parameter (this variability is
92 measured in terms of variance). Computing these Sobol’ indices therefore
93 requires to have access to an accurate mapping between the uncertain in-
94 puts and the quantities of interest. This is computationally intensive when
95 using standard Monte Carlo sampling method since this method features a
96 slow convergence rate and thus requires a large ensemble to obtain reliable
97 statistics. The cost of global sensitivity analysis is significantly reduced when
98 the forward model is replaced by a surrogate model that mimics its response
99 for the considered range of the model parameters. The formulation of such
100 a surrogate requires a limited number of model evaluations, referred to as
101 the “training set”. Then the surrogate can be evaluated multiples times at

almost no cost to evaluate uncertainties in the quantities of interest and/or perform sensitivity analysis [54, 55, 56, 57, 58].

There are various ways of formulating a surrogate. In the present work, we focus our attention on generalized polynomial chaos (gPC) expansions [59, 60, 61, 54, 62] and Gaussian process (GP) models [63, 64, 57, 55, 65, 66, 67]. The gPC-approach formulates a polynomial expansion, in which the basis is defined according to the PDF of the uncertain parameters and in which the associated weights directly relate to the statistics of the quantities of interest. This implies that by construction the quantities of interest are projected upon the same basis as the input parameters. The GP-approach adopts a different viewpoint by considering the simulated quantities of interest as a realization of a Gaussian stochastic process conditioned by the training set. This stochastic process is fully characterized with mean and covariance kernel functions, which rely on the estimation of hyperparameters. Both gPC and GP surrogates are compared in the literature for uncertainty quantification and sensitivity analysis studies [57, 58, 68, 69]. Still, the ranking between gPC and GP approaches remains problem-dependent. It is thus of great interest to compare these approaches for application in wildland fires.

In wildland fire applications, the performance of the gPC-approach has already been demonstrated within the framework of data assimilation to reduce the computational cost of sequential parameter estimation [32, 36]. However, the gPC-algorithm relied on the use of a full basis and a standard spectral projection method. Building the surrogate this way may be too costly for high-dimensional problems, i.e. when the number of uncertain parameters increases. There exists more advanced gPC-strategies in the lit-

127 erature to reduce the number of elements in the gPC basis and thus reduce
 128 the required size of the training set, see [70, 71, 72]. Due to the multiple
 129 sources of uncertainty in wildland fire models, there is a strong need to eval-
 130 uate the performance of gPC and GP approaches, i.e. for varying size and
 131 type of the training set as well as for varying parameterization and choice of
 132 the surrogate algorithms. In the present study, the objective is to determine
 133 what is the best surrogate strategy to compute Sobol’ sensitivity indices and
 134 thereby examine the relevance of the parameters that are part of the turbu-
 135 lence and fire-spotting submodel included in the wildfire spread model [47].
 136 Our objective is to identify the key parameters affecting the topology and
 137 the size of the burnt area that is simulated by an Eulerian-type fire spread
 138 model (LSFire+) and that corresponds to an idealized test case. For this
 139 purpose, we compare the performance of gPC-expansion and GP-model in
 140 their standard and sparse versions for a fixed size of the training set with dif-
 141 ferent designs of experiment (Monte Carlo random sampling, quasi-random
 142 Halton’s sequence, quadrature rule); a convergence study is carried out to
 143 determine the required size of the training set to ensure accuracy.

144 The structure of the paper is as follows. Section 2 introduces the wild-
 145 fire spread model, the main sources of uncertainty, the quantities of interest
 146 and the idealized test case study. The gPC and GP approaches are de-
 147 tailed in Section 3 along with statistical analysis tools and error metrics.
 148 Section 4 presents the results of the comparative study between gPC and
 149 GP algorithms for different types of truncation, projection and training set.
 150 Conclusions and perspectives are given in Section 5.

151 2. Wildland Fire Model and Sources of Uncertainties

152 2.1. Forward Model

153 We focus the present study on Eulerian-type wildfire spread model (LSFire+)
 154 based on level-set methods [73, 74, 75]. This is similar to the approach
 155 adopted in the ELMFIRE fire simulator [23, 76] or the WRF-SFIRE coupled
 156 fire-atmosphere system [11].

157 2.1.1. Deterministic Front Propagation

158 To represent the time-evolving burning active areas over the computa-
 159 tional domain $\Omega \subset \mathbb{R}^2$, we introduce an implicit function $\phi \equiv \phi(\mathbf{x}, t)$ as
 160 the fireline marker with $\phi : \Omega \times [0; +\infty[\rightarrow \mathbb{R}$. The fireline is identified as
 161 the contour line $\phi(\mathbf{x}, t) = \phi^*$ referred to as the “level set”. We thus denote
 162 the time-evolving two-dimensional burnt area as $\mathcal{B}(t) = \{\mathbf{x} = (x_1, x_2) \in$
 163 $\Omega \mid \phi(\mathbf{x}, t) > \phi^*\}$.

164 The temporal evolution of the level set $\phi(\mathbf{x}, t) = \phi^*$ is governed by the
 165 Eikonal equation

$$\frac{\partial \phi}{\partial t}(\mathbf{x}, t) = \mathcal{V}(\mathbf{x}, t) \|\nabla \phi(\mathbf{x}, t)\|, \quad \phi(\mathbf{x}, 0) = \phi_0(\mathbf{x}), \quad \mathbf{x} \in \Omega, \quad t \geq 0, \quad (1)$$

166 where \mathcal{V} corresponds to the ROS parameterization that is a function of the
 167 wind field $\mathbf{U}(\mathbf{x}, t)$, orography and biomass fuel conditions, and where $\phi_0(\mathbf{x})$
 168 is the initial condition at time 0. The propagation of the fireline is assumed
 169 to be directed towards the normal direction to the front.

170 *2.1.2. Random Front Formulation*

171 The stochastic approach that is adopted in the present study is based
 172 on the idea of splitting the motion of the fireline into a drifting part and a
 173 fluctuating part [47, 77, 48]. The drifting part corresponds to the resolution
 174 of the deterministic problem in Eq. (1). The fluctuating part results from a
 175 comprehensive statistical description of the dynamic system, which includes
 176 random effects in agreement with the physics of the system.

177 The motion of each burning point can be random due to the effect of
 178 turbulence and/or fire-spotting. The effective indicator function, $\phi_e(\mathbf{x}, t)$:
 179 $\mathcal{B} \times [0, +\infty[\rightarrow [0, 1]$ emerges from the superposition of the front weighted by
 180 the distribution of fluctuations around the deterministic front, i.e.

$$\phi_e(\mathbf{x}, t) = \int_{\mathcal{B}} \phi(\bar{\mathbf{x}}, t) f(\mathbf{x}; t|\bar{\mathbf{x}}) d\bar{\mathbf{x}}, \quad (2)$$

181 where $f(\mathbf{x}; t|\bar{\mathbf{x}})$ denotes the PDF of the displacement of the active burning
 182 points around the mean position $\bar{\mathbf{x}}$. An arbitrary threshold value $\phi_{e,fr}$ is used
 183 as the criterion to separate burnt area and unburnt area. The effective burnt
 184 area is therefore defined as $\mathcal{B}_e(\mathbf{x}, t) = \{\mathbf{x} \in \mathcal{B} \mid \phi_e(\mathbf{x}, t) > \phi_{e,fr}\}$.

185 Note that the PDF $f(\mathbf{x}; t|\bar{\mathbf{x}})$ is associated with two independent random
 186 variables representing turbulence and fire-spotting, with fire-spotting a down-
 187 wind phenomenon acting along the wind direction. $f(\mathbf{x}; t|\bar{\mathbf{x}})$ is expressed as

$$f(\mathbf{x}; t|\bar{\mathbf{x}}) = \begin{cases} \int_0^\infty G(\mathbf{x} - \bar{\mathbf{x}} - \ell \mathbf{n}_U; t) q(\ell; t) d\ell, & \mathbf{n} \cdot \mathbf{n}_U \geq 0, \\ G(\mathbf{x} - \bar{\mathbf{x}}; t), & \text{otherwise,} \end{cases} \quad (3)$$

189 where \mathbf{n}_U is the unit vector aligned with the mean wind direction, where
 190 $G(\mathbf{x} - \bar{\mathbf{x}}; t)$ is the PDF associated with turbulent diffusion, and where $q(\ell; t)$
 191 is the PDF associated with firebrand landing distance ℓ . We follow the
 192 same choices as in [47, 77, 48]. Hence, we assume that turbulent diffusion is
 193 isotropic and represented as a bivariate Gaussian PDF

$$G(\mathbf{x} - \bar{\mathbf{x}}; t) = \frac{1}{4\pi D t} \exp \left\{ -\frac{(x_1 - \bar{x}_1)^2 + (x_2 - \bar{x}_2)^2}{4 D t} \right\}, \quad (4)$$

194 where D is the turbulent diffusion coefficient. We also assume that the
 195 downwind distribution of the firebrands follows a log-normal distribution

$$q(\ell; t) = \frac{1}{\sqrt{2\pi} \sigma \ell} \exp \left\{ -\frac{(\ln \ell / \ell_0 - \mu)^2}{2 \sigma^2} \right\}, \quad (5)$$

196 where $\mu \equiv \mu(t) = \langle \ln \ell / \ell_0 \rangle$ and $\sigma \equiv \sigma(t) = \sqrt{\langle (\ln \ell / \ell_0 - \mu)^2 \rangle}$ are the mean
 197 and the standard deviation (STD) of $\ln \ell / \ell_0$, respectively, and where ℓ_0 is a
 198 unit reference length.

199 Since fuel ignition due to hot air and firebrands is not instantaneous, a
 200 suitable criterion related to ignition delay is introduced. This criterion is
 201 based on heating-before-burning mechanism as follows:

$$\psi(\mathbf{x}, t) = \int_0^t \phi_e(\mathbf{x}, \eta) \frac{d\eta}{\tau}, \quad (6)$$

202 where $\psi(\mathbf{x}, 0) = 0$ corresponds to the initial unburnt biomass fuel, and where
 203 τ is a reference time for ignition delay. A point \mathbf{x} is considered ignited at
 204 time t when $\psi(\mathbf{x}, t) = 1$. In this case, $\mathbf{x} \in \mathcal{B}(t)$.

205 2.1.3. Rate of Spread Submodel and Test Case Study

206 Since the focus is here on sensitivity analysis methodology, we consider
 207 a simplified version of the ROS parameterization required in Eq. (1). The
 208 maximum value of the ROS, $\mathcal{V}(x, t)$, is specified by means of Byram’s for-
 209 mula [78, 79]:

$$\mathcal{V}_0 = \frac{I}{\Delta h_c \omega_0}, \quad (7)$$

210 where I [kW m^{-1}] is the fireline intensity, Δh_c [kJ kg^{-1}] is the fuel heat of
 211 combustion and ω_0 [kg m^{-2}] is the oven-dry mass of fuel consumed per unit
 212 area in the active flaming zone. By analogy to the approach adopted in [47],
 213 the effect of the near-surface wind U on the ROS is accounted for through a
 214 corrective factor f_w as follows:

$$\mathcal{V} = \mathcal{V}_0 \frac{(1 + f_w)}{\alpha_w}, \quad (8)$$

215 where f_w is computed following the choices made in the **fire-Lib** and **Fire**
 216 **Behaviour** SDK libraries (<http://fire.org>; see also [11], in the case of the
 217 NFFL – Northern Forest Fire Laboratory – Model 9), and where α_w is a
 218 suitable angle parameter for ensuring that the maximum ROS in the upwind
 219 direction is equal to the ROS prescribed by Byram’s formula (7). This choice
 220 makes the ROS dependent on the wind direction rather than on its magnitude
 221 to constrain the well-known dominant role of the wind in the fire propagation
 222 and to allow for the emergence, if they exist, of second-order effects due to
 223 other factors.

224 In the present study, we consider an idealized test case of wildland fire.
 225 The computational domain is $7,200 \text{ m} \times 6,000 \text{ m}$. Terrain is flat. Vegetation

is homogeneous. The wind is uniform and constant. Fire ignition is represented as a circular front characterized by a radius $r_c = 130$ m and a center located at $\mathbf{x}_c = (1, 500 \text{ m}; 3, 000 \text{ m})$.

2.2. Model Input Description

The set of uncertain parameters is noted $\boldsymbol{\theta} \in \mathbb{R}^d$, where d is the number of parameters to consider for sensitivity analysis. We consider two different sets of uncertain model parameters in the present work with $d = 3$. To carry out sensitivity analysis, we need to prescribe a PDF representing the statistics of each parameter and thereby its variability; this corresponds to step. *i*) discussed in the Introduction.

2.2.1. Sensitivity analysis for macroscopic/microscopic quantities

The first set of parameters mixes macroscopic and microscopic quantities: the wind speed magnitude $\|U\|$, the fireline intensity I and the ignition delay τ . Sensitivity analysis with $\boldsymbol{\theta} = (\|U\|, I, \tau)^T$ corresponds to a preliminary step: we consider uniform marginal distributions that spanned around the mean values adopted in previous work [47, 77, 48], see Table 4.

Table 4: Ranges of variation and uniform marginal PDFs for $\boldsymbol{\theta} = (\|U\|, I, \tau)^T$. Note that the uniform distribution is formulated as $\mathcal{U}(a; b)$ with a the minimum value and b the maximum value of the parameter.

Parameter	Uniform distribution
Wind $\ U\ $ [m s^{-1}]	$\mathcal{U}(6; 14)$
Fireline intensity I [kW m^{-1}]	$\mathcal{U}(15, 000; 25, 000)$
Reference time for ignition delay τ [s]	$\mathcal{U}(0.6; 1.4)$

241

242 2.2.2. Sensitivity analysis for microscopic parameters

243 The focus of the present work is to explore the dependence of the wildfire
 244 spread model on a set of microscopic variables. We therefore determine a
 245 suitable Bayesian description for the uncertain parameters $\boldsymbol{\theta} = (\mu, \sigma, D)^T$,
 246 which relate exclusively to the fluctuating part of the forward model. Recall
 247 that μ and σ are two parameters of the log-normal PDF $q(\ell; t)$ (Eq. 5) that
 248 describes the ember landing position. Recall also that D is the diffusive coef-
 249 ficient of turbulent hot air involved in the Gaussian PDF $G(\mathbf{x} - \bar{\mathbf{x}}; t)$ (Eq. 4)
 250 that describes turbulent diffusion. Some functional dependence is explored
 251 for each parameter and their marginal PDFs are determined using a Monte
 252 Carlo random sampling. The resulting Beta-distributions are summarized in
 253 Table 5.

254 *Physical parameterization.* We assume that all turbulent processes are rep-
 255 resented in the forward model through the standalone turbulent diffusion
 256 coefficient D . We only consider turbulent fluctuations, implying that the es-
 257 timation of D is independent of the wind U . Since we consider a flat terrain
 258 and an extension of the wildland fire that is not limited to the computational
 259 domain Ω under consideration, we assume horizontal isotropy. Even though
 260 an exact estimation of D is beyond the scope of the present study, a quanti-
 261 tative estimation of D is required to carry out sensitivity analysis related to
 262 turbulence and fire-spotting. D corresponds to the turbulent heat convection
 263 generated by the fire.

264 We shall adopt for such quantitative estimation the analytical representa-

tion whose derivation can be found in [48]. Thus, D will read

$$D \simeq 0.1 \chi \left[\frac{\gamma \Delta T g h^3}{\nu \chi} \right]^{1/3} - \chi, \quad (9)$$

where χ is the air thermal diffusivity, γ is the thermal expansion coefficient, ΔT is the temperature difference in the convective cell, h is the dimension of the convective cell, g is the gravity constant and ν is the kinematic viscosity (see Table 2).

The selected parameterization for fire spotting as well is derived in [48]. Firebrand transport is characterized through the log-normal parameters μ and σ . μ describes firebrand lofting inside the convective column. The relative density and the atmospheric drag impact the buoyant forces acting on the firebrands; hence, it is appropriate to include these quantities in the definition of μ to describe the maximum allowable height for each firebrand for varying fireline intensity. The density ratio ρ_a/ρ_f also limits the maximum allowable height for each firebrand. μ is thus defined as

$$\mu = H \left(\frac{3 \rho_a C_d}{2 \rho_f^*} \right)^{1/2}, \quad (10)$$

where H [m] represents the plume height, which is related to the maximum loftable height H_p via the relation $H_p = \lambda H$, and where $\rho_f^* = \rho_f/\lambda^2$ [kg m⁻³] is the biomass fuel density that accounts for the correlation factor λ between smoke plume height and maximum allowable height for firebrands. We adopt the analytic formulation of H with respect to the fireline intensity I used

283 in [80], i.e.

$$H = \alpha_H H_{\text{ABL}} + \beta_H \left(\frac{I}{dP_{\text{f0}}} \right)^{\gamma_H} \exp \left(\delta_H \frac{N_{\text{FT}}^2}{N_0^2} \right), \quad (11)$$

284 where α_H , β_H , γ_H and δ_H are empirical constant parameters, P_{f0} [W] is the
 285 reference fire power ($P_{\text{f0}} = 10^6 \text{ W}$), H_{abl} [m] is the height of the atmospheric
 286 boundary layer (ABL), and the subscript FT stands for free troposphere.

287 The parameter σ characterizes the wind-aided transport of firebrands
 288 after they are ejected from the convective column. In a wind-driven regime
 289 of fire-spotting, the flight path of the firebrands is affected by their size, and
 290 firebrands beyond a critical size cannot be steered by the prevailing wind.
 291 This critical size is defined as the maximum liftable radius $r_{\text{max}} = \|U\|^2/g$. It
 292 is interesting to note that the dimensionless ratio $\|U\|^2/(rg)$ (r is the brand
 293 radius) is also known as the Froude number: it quantifies the balance between
 294 inertial and gravitational forces applying on firebrands. So σ is computed as

$$\sigma = \frac{1}{2z_p} \ln \left(\frac{\|U\|^2}{rg} \right). \quad (12)$$

296 Note that z_p corresponds to the p th percentile and can be estimated from the
 297 z -tables (<http://www.itl.nist.gov/div898/handbook/eda/section3/eda3671.htm>).

298 We assume that the p th percentile represents the maximum landing distance
 299 for firebrands under different situations and no ignition is possible beyond
 300 this cut-off. The cut-off criteria is chosen empirically so that $z_p = 0.45$ as
 301 in [48], which corresponds to the 67th percentile point.

302 *Statistical Description..* The following strategy is adopted to obtain a sta-
 303 tistical description of these three parameters $\{D, \sigma, \mu\}$, which depend on a

304 large set of subparameters.

305 The subparameters are perturbed around their nominal values found in
 306 the literature following uniform PDFs. To obtain a range of variation for
 307 D , we modify the parameters ΔT and h . As for parameters σ and μ , we
 308 modify the following parameters: α_H , β_H , γ_H , δ_H , H_{abl} in Eq. (11); ρ_a , ρ_f
 309 in Eq. (10); z_p and r in Eq. (12). For the parameters α_H , β_H , γ_H and δ_H ,
 310 the extrema of the uniform PDF correspond to the highest and lowest values
 311 encountered in all the possible configurations described in [80]. ΔT varies
 312 in the range [800; 923] K. For all other parameters, the extrema are defined
 313 such as adding a perturbation of 20 % to the values adopted in [48].

314 Once uniform PDFs are defined for each subparameter, we sample them
 315 through a Monte Carlo random sampling with sample size $N = 10,000$.
 316 Based on Eqs. (9)–(12), we thus obtain 10,000 realizations of the three pa-
 317 rameters of interest $\{D, \sigma, \mu\}$. We can then analyze their empirical statistical
 318 distribution by fitting the resulting histograms with different types of PDF.
 319 Figure 1 presents the fits obtained when using a Beta-distribution for each
 320 sample. We adopt such distribution due to the requirement for positiveness,
 321 limitlessness, and compatibility with the available surrogates, in particular
 322 with the gPC given the Wiener–Askey scheme, see [81]. Table 5 presents the
 323 characteristics of each Beta-distribution and the associated range of variation
 324 for each parameter in $\boldsymbol{\theta} = (\mu, \sigma, D)^T$. We recall the analytic formulation for
 325 the Beta-distribution denoted by Beta, with a and b ($a, b > 0$) the “shape
 326 parameters”:

$$\text{Beta}(x; a, b) = \frac{\Gamma(a+b) x^{a-1} (1-x)^{b-1}}{\Gamma(a)\Gamma(b)}, \quad (13)$$

for $x \in (0, 1)$, with $\Gamma(x)$ the Gamma function. To shift and/or scale the distribution, the “location” and “scale” parameters are introduced. More specifically, $\text{Beta}(x, a, b, \text{location}, \text{scale})$ is equivalent to $\text{Beta}(y, a, b)/\text{scale}$ with $y = (x - \text{location})/\text{scale}$.

2.3. Simulated Quantities of Interest

We now define two scalar indices to represent the evolution of a fire over a time period $[0; T]$. We consider first the percentage of the computational domain Ω that is burnt at a given time t :

$$A_t = \frac{\int_{\Omega} \mathcal{I}_{\mathcal{B}(t)}(x, t) dx}{|\Omega|}, \quad (14)$$

where $|\Omega|$ [m²] corresponds to the area of the computational domain and $\mathcal{I}_{\mathcal{B}(t)}$ is the indicator function of the burnt area, which returns 1 inside of the burnt area and 0 elsewhere. A_t corresponds to a normalized burnt area. However, this quantity does not give information on the topology of the fire, which can be complex in the case of fire-spotting. To overcome this limitation, we also consider an indicator S_t that describes the minimum spanning rectangle (MSR) of the burnt area over the area of the computational domain $|\Omega|$ at a given time:

$$S_t = \frac{|\text{MSR}(t)|}{|\Omega|}. \quad (15)$$

The MSR is a geometrical quantity that corresponds to the smallest rectangle within which all burnt grid points lie at a given time t . So $|\text{MSR}(t)|$ [m²] measures the area of this rectangle. As an example, Fig. 2 presents an ensemble of 100 firelines at time 50 min, where each fireline corresponds to a different set of parameters D , μ and σ (i.e. a different realization of $\boldsymbol{\theta} = (\mu, \sigma, D)^T$)

Table 5: Range of variations and Beta-distribution for $\boldsymbol{\theta} = (\mu, \sigma, D)^T$. Note that the parameters of the Beta-distribution (Eq. 13) are given in the following order: shape parameters a and b , location and scale.

Parameter	Minimum/maximum values	Beta-distribution parameters
Log-normal parameter σ	5.49–12.69	1.37 1.99 5.94 4.93
Log-normal parameter μ	7.25–98.16	3.18 7.49 7.43 94.73
Turbulent diffusion coef. D [m ² s ⁻¹]	0.23–0.47	1.19 1.20 0.23 0.23

348 obtained by sampling the Beta-distributions given in Table 5. For each fire-
 349 line, Fig. 2 shows the corresponding normalized MSR as defined in Eq. (15)
 350 at time 50 min. Low MSR values (rose colors) indicate simple topology of
 351 the fireline, while for high MSR values (yellow colors) the fireline presents
 352 more irregularities and a more complex propagation induced by turbulence
 353 and fire-spotting.

354 In this work, we analyze the time dependency of the quantities A_t and
 355 S_t by comparing them at two different times, $t_1 = 26$ min and $t_2 = 34$ min.
 356 The resulting scalar quantities (or “observables”) are noted A_1 , A_2 , S_1 and
 357 S_2 .

358 *2.4. Numerical Implementation*

359 The code **LSFire+** is developed in C and Fortran, where the turbulence
 360 and fire-spotting parametrization routines, labeled as **RandomFront 2.3b**,
 361 act as a post-processing routine at each time step in a level-set-method (LSM)
 362 code for the front propagation implemented through the library **LSMLIB** [83]
 363 and the ROS is computed by using the library **FireLib** [84]. The numer-
 364 ical library **LSMLIB** is written in Fortran2008/OpenMP. It advects the fire-
 365 line through standard algorithms for the LSM, including also fast march-
 366 ing method algorithms. The aforementioned routines are freely available at
 367 the official git repository of BCAM, Bilbao, [https://gitlab.bcamath.org/](https://gitlab.bcamath.org/atrucchia/randomfront-wrfsfire-lsfire)
 368 [atrucchia/randomfront-wrfsfire-lsfire](https://gitlab.bcamath.org/atrucchia/randomfront-wrfsfire-lsfire).

369 3. Surrogate Modeling

370 3.1. Principles and Notations

371 The objective of the present paper is to build surrogate models (or “re-
 372 sponse surfaces”) that represent how the normalized burnt area A_t or the
 373 normalized MSR S_t (the generic scalar output is noted $y \in \mathbb{R}$) changes with
 374 respect to a selection of the most relevant input parameters (the set of un-
 375 certain parameters is noted $\boldsymbol{\theta} \in \mathbb{R}^d$). The input stochastic space is defined
 376 either by $\boldsymbol{\theta} = (U, I, D)^T$ or $\boldsymbol{\theta} = (\mu, \sigma, D)^T$ (see Sec. 2.2); the size of the input
 377 stochastic space is $d = 3$.

378 The key idea of a surrogate is to replace the fire spread model $y = \mathcal{M}(\boldsymbol{\theta})$
 379 by a weighted finite sum of basis functions that can be generally expressed
 380 as

$$\hat{y}(\boldsymbol{\theta}) = \sum_{\alpha \in \mathcal{A}} \gamma_{\alpha} \Psi_{\alpha}(\boldsymbol{\theta}), \quad (16)$$

381 where the coefficients γ_{α} and the basis functions Ψ_{α} are to be determined, \mathcal{A}
 382 being the set of indices that defines the basis size. In practice, the coefficients
 383 and basis functions are calibrated by the training set (or “database”) \mathcal{D}_N
 384 that corresponds to a limited number N of forward model integrations (or
 385 “training set”) such that

$$\mathcal{D}_N = (\Theta, \mathcal{Y}) = \left\{ (\boldsymbol{\theta}^{(k)}, y^{(k)})_{1 \leq k \leq N} \right\}, \quad (17)$$

386 where $y^{(k)} = \mathcal{M}(\boldsymbol{\theta}^{(k)})$ corresponds to the integration of the forward model
 387 \mathcal{M} (LSFire+ in the present study) for the k th set of input parameters $\boldsymbol{\theta}^{(k)}$.

388 Two types of surrogate models are compared in the following: the gPC-
 389 expansion that retrieves the global forward model behavior on the one hand,

the GP regression that is a local interpolator of the forward model behavior at the training points on the other hand. Different types of surrogate are tested to determine what is the best choice in the present application. For gPC-expansion, the user needs to determine the appropriate total polynomial order of the expansion as well as the appropriate type and number of basis functions Ψ_{α} . There are also different projection strategies to compute the coefficients γ_{α} . For GP regression, the user needs to choose the type of correlation structure and to estimate its associated hyperparameters.

3.2. Generalized Polynomial Chaos (gPC) Expansion

$\boldsymbol{\theta}$ is defined in the input physical space and its counterpart in the standard probabilistic space is noted $\boldsymbol{\zeta} = (\zeta_1, \dots, \zeta_d)$, with ζ_i the random variable associated with the i th uncertain parameter θ_i in $\boldsymbol{\theta}$ characterized by its marginal PDF ρ_{θ_i} . $\boldsymbol{\theta}$ is thus rescaled in the standard probabilistic space to which the gPC framework applies.

3.2.1. Polynomial Basis

$\boldsymbol{\theta}$ is projected onto a stochastic space spanned by the orthonormal polynomial functions $\{\Psi_{\alpha}(\boldsymbol{\zeta})\}_{\alpha \in \mathcal{A}}$. The basis functions are orthonormal with respect to the joint PDF $\rho_{\boldsymbol{\zeta}}(\boldsymbol{\zeta})$, i.e.

$$\langle \Psi_{\alpha}(\boldsymbol{\zeta}), \Psi_{\beta}(\boldsymbol{\zeta}) \rangle = \int_Z \Psi_{\alpha}(\boldsymbol{\zeta}) \Psi_{\beta}(\boldsymbol{\zeta}) \rho_{\boldsymbol{\zeta}} d\boldsymbol{\zeta} = \delta_{\alpha\beta}, \quad (18)$$

with $\delta_{\alpha\beta}$ the Kronecker delta-function and $Z \subseteq \mathbb{R}^d$ the space in which $\boldsymbol{\zeta}$ evolves. In practice, the orthonormal basis is built using the tensor product of one-dimensional polynomial functions, $\Psi_{\alpha} = \phi_{\alpha_1} \dots \phi_{\alpha_d}$ with ϕ_{α_i} the

one-dimensional polynomial function. The choice for the basis functions depends on the probability measure of the random variables. According to Askey’s scheme, the Jacobi polynomials form the optimal basis for random variables following Beta-distribution, and the Legendre polynomials are the counterpart for uniform distribution [81].

Assuming that the solution of the fire spread model is of finite variance, each quantity of interest y (see Sec. 2.3) can be considered as a random variable for which there exists a gPC expansion of the form

$$\hat{y}(\boldsymbol{\theta}) = \mathcal{M}_{\text{pc}}(\boldsymbol{\theta}(\boldsymbol{\zeta})) = \sum_{\boldsymbol{\alpha} \in \mathcal{A}} \gamma_{\boldsymbol{\alpha}} \Psi_{\boldsymbol{\alpha}}(\boldsymbol{\zeta}). \quad (19)$$

$\Psi_{\boldsymbol{\alpha}}$ is the $\boldsymbol{\alpha}$ th multivariate basis function chosen in adequacy with the PDF $\boldsymbol{\rho}_{\boldsymbol{\theta}}$ associated with the parameters $\boldsymbol{\theta}$ (all random variables in $\boldsymbol{\theta}$ are assumed independent so that $\boldsymbol{\rho}_{\boldsymbol{\theta}}$ is the product of the marginal PDFs $\{\rho_{\theta_i}\}_{i=1,\dots,d}$). $\boldsymbol{\alpha} = (\alpha_1, \dots, \alpha_d)$ is a multi-index in \mathcal{A} , which identifies the components of the multivariate polynomial $\Psi_{\boldsymbol{\alpha}}$.

Note that Eq. (19) represents how the normalized burnt area A_t or the normalized MSR S_t varies according to changes in the input vector $\boldsymbol{\theta}$. Once the PDF $\boldsymbol{\rho}_{\boldsymbol{\theta}}$ is chosen, $\{\gamma_{\boldsymbol{\alpha}}\}_{\boldsymbol{\alpha} \in \mathcal{A}}$ are the unknowns to determine to build the surrogate \mathcal{M}_{pc} .

3.2.2. Truncation Strategy

For computational purposes, the sum in Eq. (19) is truncated to a finite number of terms r that is associated with the total polynomial order P of the gPC-expansion. There are several ways of choosing the number of terms r referred to as the “truncation strategy”. Note that we will use the

433 concept of “enumeration functions” in the following: a linear (or hyperbolic)
 434 enumeration function is a mapping \mathfrak{J} from \mathbb{N} to \mathbb{N}^d , which establishes a
 435 bijective mapping between a given integer i and a multi-index $\boldsymbol{\alpha}$.

436 *Linear Truncation Strategy.* The standard truncation strategy (referred to as
 437 “linear”) consists in retaining in the gPC-expansion all polynomials involving
 438 the d random variables of total degree less or equal to P . Hence, $\boldsymbol{\alpha} =$
 439 $(\alpha_1, \dots, \alpha_d) \in \{0, 1, \dots, P\}^d$. The number of terms r is therefore constrained
 440 in this linear case by the number of random variables d and by the total
 441 polynomial order P so that

$$r_{\text{lin}} = \frac{(d+P)!}{d! P!}. \quad (20)$$

442 The set of selected multi-indices for the multi-variate polynomials \mathcal{A} is de-
 443 fined as

$$\mathcal{A}_{\text{lin}} \equiv \mathcal{A}_{\text{lin}}(d, P) = \{\boldsymbol{\alpha} \in \mathbb{N}^d : |\boldsymbol{\alpha}| \leq P\} \subset \mathbb{N}^d, \quad (21)$$

444 where $|\boldsymbol{\alpha}| = \|\boldsymbol{\alpha}\|_1 = \alpha_1 + \dots + \alpha_d$ is the “total order” of the multi-index. In
 445 this case, we refer to the basis as the “full basis” for a given total polynomial
 446 order P .

447 *Hyperbolic Truncation Strategy.* As an alternative to the linear truncation
 448 strategy, the “hyperbolic” truncation strategy consists in eliminating a priori
 449 high-order interaction terms (i.e. polynomial terms involving more than one
 450 component of $\boldsymbol{\theta}$), see [70]. A more general way than Eq. (21) to define the
 451 number of terms r in the gPC expansion consists in introducing q -quasi-

452 norms:

$$\mathcal{A}_{\text{hyp}} \equiv \mathcal{A}_{\text{hyp}}(d, P, q) = \{\boldsymbol{\alpha} \in \mathbb{N}^d : \|\boldsymbol{\alpha}\|_q \leq P\}, \quad (22)$$

453 where the q -semi-norm is given by

$$\|\boldsymbol{\alpha}\|_q \equiv \left(\sum_{i=1}^d (\alpha_i)^q \right)^{1/q}. \quad (23)$$

454 The number of terms in the gPC-expansion is expressed by the cardinality of
 455 \mathcal{A} , which varies according to P and q for a fixed dimension d . The adoption
 456 of such semi-norms penalizes high-rank indices and high-order interactions.
 457 The lower the value of q , the higher the penalty in the determination of
 458 \mathcal{A} . When $q = 1$ we retrieve the linear truncation strategy and therefore
 459 a full basis of cardinality $\mathcal{A}_{\text{lin}}(d, P)$. In the following, we will study how
 460 the performance of the surrogate depends on the choice of the hyperbolic
 461 parameter $q \in [0, 1]$.

462 *Sparse Truncation Strategies.* There are alternatives to reduce the number
 463 of terms in the gPC-expansion. We will now schematically represent three
 464 of them, ordered by complexity: 1- “sequential strategy”, 2- “cleaning strat-
 465 egy”, 3- “least angle regression”.

466 1- The sequential strategy [85] consists in constructing the gPC-expansion in
 467 an incremental way, starting from the first term Ψ_0 ($K_0 = \{0\}$) and adding
 468 one term at a time in the basis ($K_{i+1} = K_i \cup \{\Psi_{i+1}\}$). The terms that are
 469 sequentially added to the basis are ordered according to the adopted enu-
 470 meration strategy (linear or hyperbolic). The response surface is therefore of
 471 increasing complexity, since the enumeration functions in both cases increase

472 the polynomial complexity when increasing the index. In the present study,
 473 the construction process is stopped when a given accuracy is achieved, or
 474 when the number of terms in the gPC-expansion reaches the maximum size
 475 of the basis r_{\max} specified by the user.

476 2- An alternative to the sequential strategy is the cleaning strategy [85], which
 477 builds a gPC-expansion containing at most r_{\max} significant coefficients, i.e. at
 478 most r_{\max} significant basis functions, starting from the full basis (still retain-
 479 ing the constraint of hyperbolic truncation if selected). The key idea of the
 480 cleaning strategy is to discard from the active basis the polynomials Ψ_{α} that
 481 are associated with coefficients of low magnitude, i.e. satisfying

$$|\gamma_{\alpha}| \leq \epsilon \cdot \max_{\alpha' \in \mathcal{A}'} |\gamma_{\alpha'}| \quad (24)$$

482 where ϵ is the significance factor set to 10^{-4} , and where \mathcal{A}' represents the
 483 current active basis. This selection procedure means that the terms in the
 484 gPC-expansion are not ordered according to the degree of the polynomial
 485 functions but instead according to the magnitude of the coefficients.

486 3- In complement to the sequential and cleaning strategies, there is a more
 487 advanced approach called least-angle regression (LAR) to select the active
 488 polynomial terms. The key idea of the LAR approach is to select at each
 489 iteration a polynomial among the r terms of the full basis (or eventually
 490 the hyperbolic-truncated basis) based on the correlation of the polynomial
 491 term with the current residual. The selected term is added to the active
 492 set of polynomials. The coefficients of the active basis are computed so
 493 that every active polynomial is equicorrelated with the current residual until
 494 convergence is reached. Thus, LAR builds a collection of surrogates that are

less and less sparse along the iterations. Iterations stop either when the full basis has been looked through or when the maximum size of the training set has been reached. When the iterations stopped, the polynomial coefficients are computed via the least-square algorithm presented below. More details can be found in [71, 70, 86].

3.2.3. Projection strategy

In this work, we focus on non-intrusive approaches based on ℓ_2 -minimization methods to numerically compute the coefficients $\{\gamma_{\alpha}\}_{\alpha \in \mathcal{A}}$ using the N snapshots from the training set \mathcal{D}_N .

Galerkin Pseudo-Spectral Projection. This Galerkin-type projection relies on the orthonormality property of the polynomial basis. Using this approach, the α th coefficient γ_{α} is computed using the definition of the inner product that is numerically approximated using tensor-based Gauss quadrature (referred to as “quadrature” in the following) as follows

$$\gamma_{\alpha} = \langle y, \Psi_{\alpha} \rangle \cong \sum_{k=1}^N y^{(k)} \Psi_{\alpha}(\boldsymbol{\zeta}^{(k)}) w^{(k)}, \quad (25)$$

where $y^{(k)} = \mathcal{M}(\boldsymbol{\theta}^{(k)})$ is the k th snapshot of the \mathcal{D}_N -database corresponding to the LSfire+ simulation for the k th quadrature root $\boldsymbol{\theta}^{(k)}$ of Ψ_{α} , and where w^k is the weight associated with $\boldsymbol{\zeta}^{(k)}$ (corresponding to $\boldsymbol{\theta}^{(k)}$ in the standard probabilistic space). When considering a full basis, $(P+1)$ is the number of quadrature roots required in each uncertain direction to ensure an accurate calculation of the integral $\langle y, \Psi_{\alpha} \rangle$. Hence, in our problem, we have $N = (P+1)^3$ simulations in the training set to build the PC surrogates through

516 Galerkin pseudo-spectral projection.

517 *Least-Square Minimization..* With this approach, the estimation of the coef-
 518 ficients $\{\gamma_{\alpha}\}_{\alpha \in \mathcal{A}}$ is done by solving a least-square minimization problem,
 519 i.e. by minimizing the approximation error between the (exact) **LSfire+**
 520 model evaluations and the PC-surrogate estimations at the points of the
 521 training set \mathcal{D}_N . The least-square projection solves a minimization problem
 522 over the given basis as follows:

$$\hat{\gamma} = \underset{\gamma \in \mathbb{R}^r}{\operatorname{argmin}} \sum_{k=1}^N \left(y^{(k)} - \sum_{\alpha \in \mathcal{A}^P} \gamma_{\alpha} \Psi_{\alpha}(\mathbf{x}^{(k)}) \right)^2 \quad (26)$$

523 which is achieved through classical linear algebra algorithms. Note that the
 524 sample size N required by this strategy for the problem to be well posed is
 525 at least equal to $(r + 1)$, where r is the number of gPC-coefficients (i.e. the
 526 cardinality of the set \mathcal{A}). Note also that least-square minimization is used
 527 here to compute the coefficients selected by the sparse truncation methods
 528 (sequential, cleaning or LAR). When using non-sparse truncation strategies,
 529 this projection method is referred to as the standard least-square (SLS) ap-
 530 proach.

531 3.2.4. Workflow scheme for constructing the gPC-expansion

532 A complete algorithm relative to the implementation of the gPC-surrogate
 533 can be summarized as follows:

- 534 1. choose the polynomial basis $\{\Psi_{\alpha}\}_{\alpha \in \mathcal{A}}$ according to the assumed marginal
 535 PDFs of the inputs $\boldsymbol{\theta} = (\|\mathbf{U}\|, I, D)^T$ or $\boldsymbol{\theta} = (\mu, \sigma, D)^T$;

- 536 2. choose the total polynomial degree P according to the complexity of
537 the physical processes;
- 538 3. truncate the expansion to r_{lin} or r_{hyp} terms corresponding to the multi-
539 index set \mathcal{A}_{lin} or \mathcal{A}_{hyp} using linear or hyperbolic truncation (r_{lin} depends
540 on d , P ; r_{hyp} depends on d , P and q with q the hyperbolic factor
541 satisfying $0 < q \leq 1$);
- 542 4. in the case of a sparse strategy (sequential, cleaning or LAR), find a
543 suitable set of multi-indices $\mathcal{A} \subset \mathcal{A}_{\text{lin, hyp}}$ with a cardinality $r \leq r_{\text{lin, hyp}}$,
544 otherwise skip this step;
- 545 5. apply a projection strategy (quadrature or least-square) to compute
546 the coefficients $\{\gamma_{\alpha}\}_{\alpha \in \mathcal{A} \subset \mathbb{N}^d}$ using $N = (P + 1)^d$ snapshots from the
547 simulation database $\mathcal{D}_{N_{\text{ref}}}$;
- 548 6. formulate the surrogate model \mathcal{M}_{pc} , which can be evaluated for any
549 new pair of parameters $\boldsymbol{\theta}^* = (\|\mathbf{U}\|^*, I^*, D^*)^T$ or $(\mu^*, \sigma^*, D^*)^T$.

550 3.3. Gaussian Process (GP) surrogate model

551 As stated by [67], a GP is a random process (here the observable from
552 the fireline evolution y) indexed over a domain (here \mathbb{R}^d), for which any
553 finite collection of process values (here $\{y(\boldsymbol{\theta}^{(k)})\}_{1 \leq k \leq N}$, $\boldsymbol{\theta}^{(k)} \in \Theta$) has a joint
554 Gaussian distribution. Concretely, let \tilde{y} be a Gaussian random process fully
555 described by its zero mean and its correlation π :

$$\tilde{y}(\boldsymbol{\theta}) \sim \text{GP}(0, \sigma_{\text{gp}}^2 \pi(\boldsymbol{\theta}, \boldsymbol{\theta}')), \quad (27)$$

556 with $\pi(\boldsymbol{\theta}, \boldsymbol{\theta}') = \mathbb{E}[\tilde{y}(\boldsymbol{\theta})\tilde{y}(\boldsymbol{\theta}')]$. In the present case, the correlation function π
557 (or kernel) is chosen as a squared exponential (also known as “RBF kernel”,

558 RBF standing for radial basis function):

$$\pi(\boldsymbol{\theta}, \boldsymbol{\theta}') = \exp\left(-\frac{\|\boldsymbol{\theta} - \boldsymbol{\theta}'\|^2}{2\ell_{\text{gp}}^2}\right), \quad (28)$$

559 where ℓ_{gp} is a length-scale representing the model output dependency be-
 560 tween two inputs $\boldsymbol{\theta}$ and $\boldsymbol{\theta}'$, and where σ_{gp}^2 is the variance of the observable.
 561 The surrogate model is thus the mean of the GP, resulting of conditioning \tilde{y}
 562 on the training set $\mathcal{Y} = \{y(\boldsymbol{\theta}^{(k)})\}_{1 \leq k \leq N}$. The quantity of interest provided
 563 by the GP-surrogate for any given $\boldsymbol{\theta}^* \in \mathbb{R}^d$ satisfies

$$y_{\text{gp}}(\boldsymbol{\theta}^*) = \sum_{k=1}^N \beta_k \pi(\boldsymbol{\theta}^*, \boldsymbol{\theta}^{(k)}), \quad (29)$$

564 where

$$\beta_k = (\boldsymbol{\Pi} + \tau_{\text{gp}}^2 \mathbf{I}_N)^{-1} (y(\boldsymbol{\theta}^{(1)}) \dots y(\boldsymbol{\theta}^{(N)}))^T, \quad (30)$$

565

$$\boldsymbol{\Pi} = (\pi(\boldsymbol{\theta}^{(j)}, \boldsymbol{\theta}^{(k)}))_{1 \leq j, k \leq N}, \quad (31)$$

566 and where τ_{gp} (referred to as the “nugget effect”) is used to avoid ill-conditioning
 567 issues for the matrix $\boldsymbol{\Pi}$. The hyperparameters $\{\ell_{\text{gp}}, \sigma_{\text{gp}}, \tau_{\text{gp}}\}$ are optimized
 568 through maximum likelihood applied to the dataset \mathcal{D}_N using a basin hop-
 569 ping technique [87].

570 3.4. Design of Experiments

571 We build several datasets to analyze the performance of the gPC- and GP-
 572 surrogates in an extensive way in Section 4; these datasets are summarized
 573 in Table 6. Note that estimating the generalization error of the surrogate

574 model requires the use of an independent dataset, that is why we use a
575 Monte Carlo random sampling including $N = 216$ members for validation.
576 Note also that the Halton’s low-discrepancy sequence is involved in this work
577 in order to explore the hypercube defined by the distribution of the uncertain
578 parameters. This design of experiment will be compared to a tensor-based
579 Gauss quadrature in terms of performance of the surrogate model. The reader
580 shall refer to Section 2.2 for more details on the range of variation and the
marginal PDFs of each uncertain parameter.

Table 6: Datasets \mathcal{D}_N of **LSfire+** simulations used in this work for building surrogates (“training”) or for validating them (“validation”).

Sampling Strategy	Purpose	Sample size
$\boldsymbol{\theta} = (\ \mathbf{U}\ , I, D)^T$		
Halton’s sequence	Training	216
Monte Carlo random sampling	Validation	216
$\boldsymbol{\theta} = (\mu, \sigma, D)^T$		
Halton’s sequence	Training	216
Quadrature rule	Training	216
Monte Carlo random sampling	Validation	216

581

582 3.5. Error Metrics

583 In the present study, two error metrics are used to assess the quality of the
584 surrogate predictions: the empirical error between the surrogate prediction
585 and the **LSfire+** model prediction (also known as “training error”) on the
586 one hand, and the Q_2 predictive coefficient [55] on the other hand.

587 3.5.1. Empirical Error ϵ_{emp}

588 The truncation of the gPC-expansion can eventually introduce an approx-
589 imation error at the training points, which can be computed posterior to the

590 surrogate construction. This empirical error denoted by ϵ_{emp} reads

$$\epsilon_{\text{emp}} = \frac{1}{N} \sum_{k=1}^N (y^{(k)} - \hat{y}^{(k)}), \quad (32)$$

591 with $y^{(k)}$ the k th element of the training set \mathcal{D}_N (either the Halton’s low
 592 discrepancy sequence or the quadrature database, see Table 6) and $\hat{y}^{(k)}$ the
 593 corresponding value predicted by the surrogate for the same element of the
 594 training set.

595 However, this error estimator has several drawbacks. First, the GP-model
 596 (built without noise in the kernel) is an interpolator so that the approxima-
 597 tion error is expected to be $\epsilon_{\text{emp}} = 0$. Second, this estimator may severely
 598 underestimate the magnitude of the mean square error. When the size of the
 599 training set N comes closer to the cardinality of the gPC-expansion \mathcal{A} , ϵ_{emp}
 600 may tend to zero, while the actual mean square error does not; this issue is
 601 known as “overfitting”.

602 3.5.2. Predictive coefficient Q_2

We require a more robust error estimator suitable for both gPC-expansion
 and GP-model. In this work, we use the Q_2 predictive coefficient based
 on cross-validation. The computation of Q_2 relies on two distinct datasets:
 the current training set \mathcal{D}_N (either the Halton’s sequence or the quadrature
 database) and a Monte Carlo sample $\mathcal{D}_{N_{\text{ref}}}$ that is independent of the surro-
 gate construction and that is therefore referred to as the “validation dataset”.

Q_2 is computed as

$$Q_2 = 1 - \frac{\sum_{k=1}^{N_{\text{ref}}} (y^{(k)} - \hat{y}^{(k)})^2}{\sum_{k=1}^{N_{\text{ref}}} (y^{(k)} - \bar{y}_{\text{ref}})^2}, \quad (33)$$

with $y^{(k)}$ the k th element of the Monte Carlo sample $\mathcal{D}_{N_{\text{ref}}}$, $\hat{y}^{(k)}$ the surrogate prediction for the same element of $\mathcal{D}_{N_{\text{ref}}}$ and \bar{y}_{ref} the empirical mean over the Monte Carlo sample $\mathcal{D}_{N_{\text{ref}}}$. Note that computing Q_2 , the training set \mathcal{D}_N is only used to construct the surrogate model and to obtain the estimation \hat{y} of the quantity of interest y . The target value for Q_2 is 1.

3.6. Statistical Analysis

Once the surrogates are available for the different observables (A_1 , A_2 , S_1 , S_2 – see Section 2.3), the statistics of the quantities of interest can be obtained. For the gPC-expansion, they can be derived analytically from the coefficients. For the GP-surrogate, we evaluate the surrogate predictions over a new dataset $\mathcal{D}_{N_{\text{sample}}}$ of size $N_{\text{sample}} = 10,000$ that is a subset of \mathbb{R}^3 and that is obtained using a standard Monte Carlo random sampling; this dataset is only used as input to the surrogate model and not to **LSfire+**.

616 3.6.1. Estimation of Statistical Moments

617 The mean value and STD of the observable y can be estimated as

$$\mu_{\hat{y}} = \frac{1}{N_{\text{sample}}} \sum_{k=1}^{N_{\text{sample}}} \hat{y}^{(k)}, \quad (34)$$

$$\sigma_{\hat{y}} = \sqrt{\frac{1}{N_{\text{sample}} - 1} \sum_{k=1}^{N_{\text{sample}}} (\hat{y}^{(k)} - \mu_{\hat{y}})^2}, \quad (35)$$

618 with $\hat{y}^{(k)}$ the k th element of the dataset $\mathcal{D}_{N_{\text{sample}}}$ containing the surrogate
619 evaluations over the aforementioned Monte Carlo sampled points.

620 Using the gPC-surrogate, the statistical moments can be derived ana-
621 lytically from the coefficients $\{\gamma_{\alpha}\}_{\alpha \in \mathcal{A} \subset \mathbb{N}^d}$ such that the mean and the STD
622 read:

$$\mu_{\hat{y}_{\text{pc}}} = \gamma_0, \quad (36)$$

$$\sigma_{\hat{y}_{\text{pc}}} = \sqrt{\sum_{\substack{\alpha \in \mathcal{A} \subset \mathbb{N}^d \\ \alpha \neq 0}} \gamma_{\alpha}^2}. \quad (37)$$

623 3.6.2. Sensitivity Analysis Diagnostics

624 Sobol' indices [53, 49] are commonly used for sensitivity analysis based
625 on variance analysis. They provide the quantification of how much of the
626 variance in the quantity of interest is due to the variance in the input param-
627 eters assuming (1) these input random variables are independent and (2) the
628 random output is squared integrable.

629 The variance of an output random variable y denoted by $\mathbb{V}[y]$ can be

630 decomposed as

$$\mathbb{V}[y] = \sum_{i=1}^d \mathbb{V}_i(y) + \sum_{j=i+1}^d \mathbb{V}_{ij}(y) + \cdots + \mathbb{V}_{1,2,\dots,d}(y), \quad (38)$$

631 where $\mathbb{V}_i(y) = \mathbb{V}[\mathbb{E}(y|\theta_i)]$, $\mathbb{V}_{ij}(y) = \mathbb{V}[\mathbb{E}(y|\theta_i, \theta_j)] - \mathbb{V}_i(y) - \mathbb{V}_j(y)$ and more
 632 generally,

$$\mathbb{V}_I(y) = \mathbb{V}[\mathbb{E}(y|\theta_I)] - \sum_{J \subset I \text{ s.t. } J \neq I} \mathbb{V}_J(y), \quad \forall I \subset \{1, \dots, d\} \quad (39)$$

Based on this variance decomposition, the first-order Sobol' index S_i associated with the i th parameter of $\boldsymbol{\theta}$ is given by

$$S_i = \frac{\mathbb{V}_i(y)}{\mathbb{V}(y)}, \quad (40)$$

and corresponds to the ratio of the output variance $\mathbb{V}(y)$ that is uniquely related to the i th input parameter; S_i ranges between 0 and 1. The corresponding total Sobol' index S_{T_i} measures the whole contribution of the i th input parameter (including *interactions with other parameters* of $\boldsymbol{\theta}$) on the output variance. Its definition reads

$$S_{T_i} = \sum_{\substack{I \subset \{1, \dots, d\} \\ I \ni i}} S_I. \quad (41)$$

633 By definition, $S_{T_i} \geq S_i$. If both first-order and total indices are not equal,
 634 this means that the input parameter θ_i share some interactions with other
 635 parameters of $\boldsymbol{\theta}$.

636 For the GP-surrogate approach, Sobol' indices are stochastically esti-

637 mated using Martinez' formulation since this estimator is stable and provides
 638 asymptotic confidence intervals for first-order and total-order indices [88].

639 For the gPC-expansion approach, Sobol' indices can be directly derived
 640 from the gPC-coefficients. For the i th component of the input random vari-
 641 able $\boldsymbol{\theta}$, the Sobol' index $\mathbb{S}_{\text{pc},i}$ reads:

$$\mathbb{S}_{\text{pc},i} = \frac{1}{(\sigma_{\hat{\mathbf{y}}_{\text{pc}}})^2} \sum_{\substack{\boldsymbol{\alpha} \in \mathcal{A}_i \subset \mathbb{N}^d \\ \boldsymbol{\alpha} \neq \mathbf{0}}} (\gamma_{\boldsymbol{\alpha}})^2, \quad (42)$$

642 where $\sigma_{\hat{\mathbf{y}}_{\text{pc}}}$ is the STD computed in Eq. (37), and where \mathcal{A}_i is the set of
 643 multi-indices selected in \mathcal{A} such that the computation of $\mathbb{S}_{\text{pc},i}$ only includes
 644 terms that depend on the input variable θ_i , namely

$$\mathcal{A}_i = \{\boldsymbol{\alpha} \in \mathbb{N}^d, |\boldsymbol{\alpha}| \leq P \mid \alpha_i > 0, \alpha_{k \neq i} = 0\}. \quad (43)$$

645 3.7. Numerical Implementation

646 The GP implementation relies on the Python package *scikit-learn* [89]
 647 (see <http://scikit-learn.org/>). The gPC-implementation relies on the Python
 648 package *OpenTURNS* [85] (see www.openturns.org). The *batman* [90] Python
 649 package is used to build datasets and perform statistical analysis.

650 4. Results

651 The objective of this study is two-fold. First, we provide an extensive
 652 comparison of the performance of different surrogate strategies (see Table 7)
 653 for a given training set \mathcal{D}_N ; We evaluate their impact on the predicted
 654 quantities of interest A_t and S_t in terms of mean value and STD, but also their

655 impact on the predicted Sobol’ sensitivity indices. This extensive analysis
656 is carried out for the case $\boldsymbol{\theta} = (\mu, \sigma, D)^T$, related to the fluctuating part of
657 the model. Second, we use this framework to rank the uncertain parameters,
658 either $\boldsymbol{\theta} = (\|U\|, I, \tau)^T$ or $\boldsymbol{\theta} = (\mu, \sigma, D)^T$, by order of importance and identify
659 the most influential input parameters.

660 4.1. Comparison of surrogate performance

661 4.1.1. Error assessment

662 Table 8 presents the error metrics (i.e. the ϵ_{emp} empirical error and the
663 Q_2 predictive coefficient) obtained for different types of surrogate (gPC on
664 the one hand, and GP on the other hand) with respect to $\boldsymbol{\theta} = (\mu, \sigma, D)^T$ but
665 for a given size of the training set $N = 216$. The performance of the gPC-
666 surrogate is analyzed in details for varying truncation and projection schemes
667 summarized in Table 7; the GP-surrogate is obtained using a standard RBF
668 kernel and is considered here as a basis for comparison in order to evaluate
669 the quality of the gPC-surrogates. For each approach, one surrogate model
670 is built for each of the four observables $\{A_1, A_2, S_1, S_2\}$ corresponding to the
671 two quantities of interest A_t and S_t at times $t_1 = 26$ min and $t_2 = 34$ min.

672 In Table 8 we first focus on the results obtained with linear truncation
673 ($q = 1$), meaning that the basis of polynomial functions is full for a given
674 total polynomial order P . Figure 3 (right figure of each pair) presents cor-
675 responding scatter plots (referred to as “adequacy plots”) of the surrogate
676 predictions with respect to the physical model predictions. These plots quan-
677 tify the adequacy of the surrogate to the physical model at the training points
678 in terms of predicted burnt area ratio A_2 . It is found that the Q_2 predictive
679 coefficient is over 0.9 only for the LAR and cleaning sparse methods for all

680 observables. The empirical error is of the same order of magnitude, varying
 681 between 10^{-3} for the MSR ratio S_t and 10^{-4} for the burnt area ratio A_t . Note
 682 that for a given observable at a given time, there is no significant difference
 683 among the surrogate strategies in terms of empirical error. We therefore fo-
 684 cus the following analysis on the standalone Q_2 predictive coefficient. Note
 685 also that the performance of each surrogate is time independent since for a
 686 given observable, the Q_2 predictive coefficient is similar at times t_1 and t_2 .
 687 We therefore focus on results at time t_2 in the following.

688 When moving to hyperbolic truncation schemes ($q = 0.75$ or $q = 0.5$), we
 689 reduce a priori the number of coefficients to compute in the gPC-expansion,
 690 while the size of the training set remains the same ($N = 216$). The lower the
 691 value of q , the smaller the number of gPC-coefficients r . Figure 4 (right plot
 692 of each pair) presents adequacy plots for hyperbolic truncation with $q = 0.5$;
 693 this is to compare to the adequacy plots obtained for linear truncation in
 694 Figure 3 (right plot of each pair). Results show that the performance of the
 695 quadrature approach does not improve when q decreases. In the opposite,
 696 the performance of the SLS approach improves and features a Q_2 predictive
 697 coefficient over 0.9 for A_2 and over 0.8 for S_2 when using hyperbolic trunca-
 698 tion. This improvement is also noticeable in Figure 4 (right plot of each pair),
 699 where hyperbolic truncation allows to better represent the model response
 700 for low values of the burnt area ratio ($A_2 < 0.03$). The sequential sparse
 701 method also provides better results for a hyperbolic coefficient $q = 0.5$. The
 702 performance of LAR and cleaning sparse methods remains similar as in the
 703 linear case $q = 1$.

704 LAR appears as the most accurate gPC strategy and has a Q_2 predic-

705 tive coefficient that is similar to that obtained with the GP-model based on
706 RBF kernel. Hyperbolic truncation does not add much value to the results
707 compared to linear truncation, except for the SLS strategy. This may be
708 explained by the fact that the terms that are important to retain in the
709 gPC-expansion are not located in an isotropic way in the three dimensions
710 ($d = 3$). It is therefore of interest to identify which polynomial terms are
711 important to keep in the basis in order to obtain a good performance of the
712 surrogate in each of the three dimensions.

713 4.1.2. Sensitivity of gPC-surrogates to total polynomial order P

714 In Table 8, the results for SLS and LAR methods are obtained by choosing
715 the optimal value of the total polynomial order P in the sense that the
716 surrogate was obtained by finding the value of P that maximizes the Q_2
717 predictive coefficient; P varying between 1 and 14. Recall that the total
718 polynomial order P determines the size of the full basis used to construct
719 the surrogate when using linear truncation. The SLS method considers the
720 full basis, while the LAR method selects the most influential terms among
721 the full basis. Since the size of the training set is fixed to $N = 216$ and since
722 $(P + 1)^3 = 216$ for $P = 5$, we know that the problem becomes ill-posed for
723 a full basis when the total polynomial order is over 5. This is not an issue
724 for LAR since it selects inline the influential coefficients in the basis. It is
725 therefore of interest to investigate if the LAR method features an improved
726 performance when $P > 5$.

727 Figure 5 presents the Q_2 predictive coefficient for P varying between 1
728 and 14 for SLS and LAR surrogates obtained for the burnt area ratio A_2 .
729 As expected, Fig. 5a shows that the best performance of the SLS method

730 with linear truncation is obtained for $P = 5$ and that it degrades very fast
 731 when increasing P (the Q_2 predictive coefficient is below 0.4 for $P > 6$).
 732 When moving to hyperbolic truncation with $q = 0.5$, Fig. 5c shows that
 733 the Q_2 predictive coefficient remains over 0.4 for $P > 5$. The resulting
 734 surrogate is therefore improved in this configuration as already pointed out in
 735 Table 8. Hyperbolic truncation allows the SLS approach to include high-order
 736 polynomials in the basis without generating an ill-posed problem (i.e. without
 737 having more coefficients to compute than the size N of the training set). Still,
 738 results show that the Q_2 predictive coefficient does not follow a monotonically
 739 increasing function toward the target value 1 in this hyperbolic configuration;
 740 this configuration is therefore not robust. In the opposite, the LAR method
 741 shows a monotonic convergence towards the target value 1 when increasing
 742 P in Figs. 5b–d. A good performance of LAR is obtained for $P = 10$ for
 743 both linear and hyperbolic truncation schemes.

744 This sensitivity study shows that a total polynomial order P higher than 5
 745 is required to build the response surface of the burnt area ratio. Similar re-
 746 sults are obtained for the MSR ratio (not shown here). This demonstrates
 747 the benefits from sparse schemes when having a fixed and limited training
 748 set \mathcal{D}_N . Improving the performance of the SLS approach using linear trunca-
 749 tion would require a higher total polynomial order P and therefore a larger
 750 training set.

751 4.1.3. Identification of the influential gPC-coefficients

752 Figure 3 (left figure of each pair) presents a three-dimensional schematic
 753 (referred to as “sparsity plot”) of the coefficients retained in the gPC-expansion
 754 using linear truncation, each dimension corresponding to one stochastic/uncertain

755 dimension. The three dimensions are here the turbulent diffusion coefficient
756 D and the lognormal parameters μ and σ .

757 Quadrature and SLS methods have the same full basis for a given poly-
758 nomial order P (here $P = 5$ since the size of the training set is $N = 216$);
759 they are associated with a typical “pyramidal” sparsity plot, where the first
760 coefficient corresponding to the mean estimate of the burnt area ratio A_2
761 has the highest magnitude (approximately equal to 0.04). For sparse meth-
762 ods (LAR, cleaning, sequential), the number of coefficients is significantly
763 reduced since the terms with the least impact are automatically filtered out
764 of the sparse basis. The sparsity plot has no longer a “pyramidal” shape.
765 LAR and sequential strategies feature instead a two-dimensional structure
766 (along the vertical plane) indicating that the burnt area ratio A_2 is not sen-
767 sitive to the third dimension, here the lognormal parameter μ , but only to
768 the lognormal parameter σ and to the turbulent diffusion coefficient D . Only
769 the cleaning strategy retains a three-dimensional structure by accounting for
770 interaction terms involving the lognormal parameter μ . This highlights the
771 presence of influential interaction terms involving several parameters. How-
772 ever, all sparse strategies indicate that one direction is dominant since the
773 number of coefficients in this direction is high and the basis terms can go
774 up to a total polynomial order $P = 12$ in the case of cleaning and $P = 8$ in
775 the case of LAR (instead of the constrained $P = 5$ for quadrature and SLS).
776 This dominant direction corresponds to the lognormal parameter σ .

777 Note that Figure 4 (left figure of each pair) presents similar plots as Fig-
778 ure 3 (left figure of each pair) but for hyperbolic truncation with $q = 0.5$.
779 The magnitude of the coefficients does not change for quadrature, explaining

780 why hyperbolicity does not improve the performance of the surrogate based
781 on quadrature. This is not the case of SLS, which now features high magni-
782 tude for the coefficients along the direction D for polynomial terms having
783 a degree between 4 and 8. This highlights the need to have polynomials
784 of higher degree to capture underlying physical processes. Still, SLS with
785 hyperbolicity is not sufficient to capture the same structure as sparse meth-
786 ods. Note that sparse methods converge to the same structure using linear or
787 hyperbolic truncation schemes, indicating the robustness of these methods.

788 The influence of the three parameters on the behavior of the burnt area ra-
789 tio A_2 can be quantified using Sobol' sensitivity indices. Table 9 presents the
790 Sobol' indices using sparse methods and linear truncation for the burnt area
791 ratio A_2 (same results are obtained using hyperbolic truncation with $q = 0.5$
792 – not shown here). Table 10 presents similar quantities for the MSR ratio S_2 .
793 Results confirm that the lognormal parameter σ is the most influential one
794 for both quantities of interest A_2 and S_2 with a first-order sensitivity index
795 above 0.98 for A_2 and above 0.92 for S_2 . This means that more than 90 % of
796 the variance in A_2 and S_2 is explained by uncertainties in the lognormal pa-
797 rameter σ . Results also show interaction effects are limited but still present
798 between the lognormal parameter σ and the turbulent diffusion parameter
799 D as foreseen in sparsity plots. Note that all sparse gPC-surrogates as well
800 as the GP-model exhibit the same global trend. The main differences lie in
801 the relevance of the lognormal parameter μ . LAR and sequential strategies
802 cut out any contribution of μ in the variability of the predicted quantities
803 of interest. This is not the case of the cleaning strategy that has a non-zero
804 total Sobol' index for μ as the GP-model.

805 We can evaluate the impact of the choice in the surrogate strategy on
806 the predicted mean and STD estimates of the quantities of interest. Ta-
807 ble 11 presents the mean and STD estimate of the burnt area ratio A_2 and
808 of the MSR ratio S_2 obtained for different gPC- and GP-surrogates. Re-
809 sults show the consistency of the statistical moments obtained using sparse
810 gPC-expansions and GP-model for both A_2 and S_2 . The SLS approach using
811 linear truncation is able to retrieve accurate mean and STD estimates (about
812 1 % deviation with respect to GP-model predictions). In the opposite, the
813 quadrature approach provides mean and STD estimates with more than 10 %
814 deviation with respect to GP-model predictions.

815 This highlights the importance of having high-order polynomial terms in
816 some uncertain directions to build an accurate gPC-expansion and have ac-
817 curate estimate of the statistical moments in the present study. These direc-
818 tions can be identified using Sobol' sensitivity indices. Sparse gPC-strategies
819 are relevant to address such issues due to the flexibility of selecting the most
820 influential polynomial terms during the construction of the surrogate (linear
821 and hyperbolic schemes are defined a priori).

822 4.1.4. *Sensitivity to the size of the training set*

823 So far the analysis was obtained for a fixed training set of size $N = 216$
824 (generated using Halton's low discrepancy sequence or tensor-based Gauss
825 quadrature in the case of quadrature). It is of interest to study if the same
826 level of accuracy could be obtained for sparse gPC-surrogates built with a
827 reduced training set ($N < 216$). To answer this question, we provide a con-
828 vergence test for a training size N varying between 10 and 216 with respect
829 to the observable S_2 . For each size of the training set, a LAR gPC-surrogate

is built and cross-validated using the available Monte Carlo database (Table 3.4) through the computation of the Q_2 predictive coefficient. We carry out this convergence test for different truncation strategies, i.e. for different levels of hyperbolicity $q \in \{1, 0.75, 0.5\}$. Figure 6 presents the evolution of Q_2 with respect to the size of the training set N . Results show the convergence of Q_2 to a constant value for $N > 100$. Linear truncation and hyperbolic truncation ($q = 0.5$) provide similar performance for $N > 100$. As before, we note that the hyperbolic solution obtained using $q = 0.75$ is not the best option.

4.2. Analysis of the physical model predictions

Results show that the LAR gPC-strategy features a good performance. In the following, we will use this strategy to further analyze the fire-spotting and turbulence submodel included in **LSFire+**. We summarize in Table 13 and Table 15 the error metrics as well as the mean and STD estimate of the burnt area ratio A_2 and of the MSR ratio S_2 at time t_2 for the two sets of uncertain parameters $\boldsymbol{\theta} = (\|U\|, I, \tau)^T$ and $\boldsymbol{\theta} = (\mu, \sigma, D)^T$, respectively. Table 12 and Table 14 present the corresponding Sobol' Indices. Note that the following analysis holds for any time t since we show that results can be considered as time-independent. Note also that the empirical error ϵ_{emp} and the Q_2 predictive coefficient are in acceptable range for all tested configurations; we focus here on the physics of the problem.

Sobol' sensitivity indices order by relevance each parameter. In the case $\boldsymbol{\theta} = (\|U\|, I, \tau)^T$, a clear dominance of the wind speed $\|U\|$ is observed for the considered range of the fireline intensity I . This is a rather interesting result, since the normalization performed on the ROS model (i.e. parameter

855 α_w in Eq. 7) makes the propagation of the deterministic fireline depending
 856 solely on the orientation of the wind vector and not on its magnitude. This
 857 means that the wind has a more general and fundamental role as reflected
 858 also in the enhancement of fire-spotting and secondary fire generation.

859 The ballistic term σ in Eq. (5) strongly depends on the value of $\|U\|$.
 860 This is in line with the results of the second set of input parameters. In the
 861 case $\theta = (\mu, \sigma, D)^T$, σ is the most influential parameter when considering
 862 Sobol' indices, far above D and μ (in order of relevance). The trend for the
 863 observables A_t and S_t is comparable, still S_t gives slightly more relevance to μ
 864 and D inputs than A_t . As expected, for both parameter sets, the mean of the
 865 S_2 -observable is larger than that of A_2 . Its STD is also larger. Uncertainties
 866 in $\{\|U\|, I, \tau\}$ induce a more significant spread of the fireline position and
 867 shape compared to uncertainties in $\{\mu, \sigma, D\}$. This is due to the fact that in
 868 the first case we also vary the ember ignition time scale.

869 In summary, these results highlight the importance of the mean wind
 870 factor, on the main fire propagation but also on the generation of secondary
 871 fires. This is consistent with the phenomenology of wildland fires and with
 872 the process of fire-spotting. In particular, fire-spotting refers to independent
 873 ignitions located far away from the main fireline. This process is accounted
 874 in the model via the lognormal parameter σ . The importance of σ is a proper
 875 mathematical feature of the adopted lognormal PDF for firebrand landing
 876 distance, since it controls the tail of the density function, the kurtosis of the
 877 lognormal density being equal to $e^{4\sigma^2} + 2e^{3\sigma^2} + 3e^{2\sigma^2} - 3$. Hence this study
 878 shows that the new submodel correctly includes the double role of the mean
 879 wind, enhancing the propagation of the main fireline on the one hand, and

880 carrying away firebrands for secondary ignitions on the other hand.

881 5. Discussion and Conclusions

882 This study presents an extensive comparative study of surrogate ap-
883 proaches to the nonlinear and multi-scale problem of turbulence and fire-
884 spotting in wildland fire modeling, fire-spotting being a random process in
885 which firebrand generation, emission and landing distance are intrinsically
886 governed by the fire strength. A surrogate modeling approach is useful to
887 analyze in a cost-effective way, how the fireline position and topology change
888 according to variations in the input parameters for the new physical sub-
889 model introduced by Pagnini et al [45, 46, 47, 48] based on a randomized
890 representation of the fireline. Results are presented from both algorithmic
891 and physical perspectives. From an algorithmic viewpoint, it is of interest to
892 compare several approaches to carry out global sensitivity analysis and to se-
893 lect which ones are accurate and computationally efficient. From a wildland
894 fire perspective, uncertainty quantification and sensitivity analysis is a good
895 practice to analyze any new submodel, spot unimportant parameters and
896 identify which parameters are dominant for obtaining a good representation
897 of turbulence and fire-spotting.

898 In this work, fast surrogate models based on generalized Polynomial
899 Chaos (gPC) and Gaussian Process (GP) were used to limit the required
900 number of physical model evaluations to at least 100. We analyzed the per-
901 formance of different formulations of the gPC-surrogate in terms of design of
902 experiments (how to choose the training points? how many training points
903 are required to achieve a certain accuracy?), polynomial basis structures

904 (how to select the influential terms of the polynomial basis?) and projec-
 905 tion schemes (how to compute the coefficients of the gPC-expansion?). The
 906 generalization error of these surrogates was classically estimated using the
 907 Q_2 predictive coefficient. Sparse gPC-methods have shown their accuracy in
 908 line with the GP model based on RBF kernel, but with a less cumbersome
 909 representation for Sobol' indices and statistical moments. Sparse methods
 910 provide more flexibility to select high-order polynomial terms in a given di-
 911 rection of the uncertain space, without requiring more physical model evalu-
 912 ations and therefore without increasing the computational cost of sensitivity
 913 analysis. The best performance for the gPC-surrogate was obtained using a
 914 sparse least-angle regression (LAR) with a training set built using a Halton's
 915 low discrepancy sequence. Using this approach, the new parametrization
 916 **RandomFront 2.3b** for turbulence and fire-spotting was found to be a non-
 917 linear model with a remarkable range of variations in the size and topology
 918 of the fire due to uncertainties in its input parameters. There is a clear
 919 dominance of the lognormal parameter σ characterizing firebrand downwind
 920 transport and of the wind magnitude $\|U\|$, which confirms that fire-spotting
 921 is a wind-driven, ballistic phenomenon.

922 Several issues can be met when building a robust surrogate model. First,
 923 when the problem is multi-scale, i.e. when uncertain parameters have corre-
 924 lation length-scales differing by several order of magnitudes. Sparse methods
 925 may filter out the less influential parameters. The LAR-based gPC surrogate
 926 was found to filter out the information coming from parameters with large
 927 length-scale. The cleaning-based surrogate proved to preserve these informa-
 928 tion, which may be important in a multi-scale problem such as fire-spotting.

929 Second, when choosing how to sample the stochastic space and construct the
930 training set. Standard projection schemes such as tensor-grid Gauss quadra-
931 ture and standard least-square methods have shown their limitations: a large
932 part of the training set was wasted in regions of the parameter space far
933 from the nonlinear processes to be explored. In the opposite, sparse methods
934 based on least-square projection were found to identify in which stochastic
935 direction the physical processes are more complex and require higher order
936 polynomials or high-order interaction terms. Using hyperbolic truncation
937 was not flexible enough for this purpose.

938 The increasing strength and occurrence of megafires due to climate change
939 calls for the development of new tools for the prediction of fire occurrence,
940 growth and frequency at regional scales. Reliable wildland fire spread models
941 are a promising approach to provide short-term variability of fire danger.
942 Statistical methods such as uncertainty quantification and sensitivity analysis
943 also have an important role to play [91, 92, 93]. Present work pushes toward
944 the integration of fire-spotting into regional-scale operational wildland fire
945 spread simulators. This is the main direction of the future developments of
946 this research. Future work will also include the extension of the surrogate
947 approaches to vectorial inputs and outputs, in order to analyze the sensitivity
948 of the fire behavior to a wind field and to describe the fire situation as a map
949 instead of a scalar variable.

950 *Acknowledgements.* This research is supported by the Basque Government
951 through the BERC 2014–2017 and BERC 2018–2021 programs, by the Span-
952 ish Ministry of Economy and Competitiveness MINECO through BCAM
953 Severo Ochoa accreditations SEV-2013-0323 and SEV-2017-0718 and through

954 project MTM2016-76016-R "MIP", and by the PhD grant "La Caixa 2014".
 955 The authors acknowledge EDF R&D for their support on the OpenTURNS
 956 library. They also acknowledge Pamphile Roy and Matthias De Lozzo at
 957 CERFACS for helpful discussions on *batman* and *scikit-learn* tools.

958 References

- 959 [1] D. Viegas, Forest Fire Propagation, Philosophical Transactions: Math-
 960 ematical, Physical and Engineering Sciences 356 (1998) 2907–2928.
- 961 [2] R. Linn, J. Reisner, J. Colman, J. Winterkamp, Studying wildfire be-
 962 havior using FIRETEC, Int. J. Wildland Fire 11 (2002) 233–246.
- 963 [3] W. Mell, M. Jenkins, J. Gould, P. Cheney, A physics-based approach to
 964 modelling grassland fires, Int. J. Wildland Fire 16 (2007) 1–22.
- 965 [4] S. Strada, C. Mari, J. B. Filippi, F. Bosseur, Wildfire and the atmo-
 966 sphere: Modelling the chemical and dynamic interactions at the regional
 967 scale, Atmos. Environ. 51 (2012) 234–249.
- 968 [5] M. Finney, J. Cohen, S. McAllister, W. Matt Jolly, On the need for a
 969 theory of wildland fire spread, Int. J. Wildland Fire 22 (1) (2013) 25–36.
- 970 [6] S. McAllister, M. Finney, Convection ignition of live forest fuels, Fire
 971 Safety Science 11 (2014) 1312 – 1325. doi:10.3801/IAFSS.FSS.
 972 11-1312.
- 973 [7] T. L. Clark, M. A. Jenkins, J. Coen, D. Packham, A coupled
 974 atmospheric-fire model: convective feedback on fire-line dynamics, J.
 975 Appl. Meteor. 35 (1996) 875–901.

- 976 [8] B. E. Potter, A dynamics based view of atmosphere-fire interactions,
977 Int. J. Wildland Fire 11 (2002) 247–255.
- 978 [9] B. E. Potter, Atmospheric interactions with wildland fire behaviour - i.
979 basic surface interactions, vertical profiles and synoptic structures, Int.
980 J. Wildland Fire 21 (2012) 779–801.
- 981 [10] B. E. Potter, Atmospheric interactions with wildland fire behaviour - ii.
982 plume and vortex dynamics, Int. J. Wildland Fire 21 (2012) 802–817.
- 983 [11] J. Mandel, J. D. Beezley, A. K. Kochanski, Coupled atmosphere-
984 wildland fire modeling with WRF 3.3 and SFIRE 2011, Geosci. Model.
985 Dev. 4 (2011) 591–610.
- 986 [12] J. B. Filippi, X. Pialat, C. B. Clements, Assessment of ForeFire/Meso-
987 NH for wildland fire/atmosphere coupled simulation of the FireFlux
988 experiment, Proc. Combust. Inst. 34 (2013) 2633–2640.
- 989 [13] D. Viegas, L. Pita, Fire spread in canyons, Int. J. Wildland Fire 13 (274)
990 (2004) 1–22.
- 991 [14] D. Viegas, A. Simeoni, Eruptive behaviour of forest fires, Fire Technol.
992 47 (2) (2010) 303–320.
- 993 [15] M. Nijhuis, Forest fires: Burnt out, Nature 489 (2012) 352–354.
- 994 [16] M. Cruz, A. Sullivan, J. Gould, N. Sims, A. Bannister, J. Hollis, R. Hur-
995 ley, Anatomy of a catastrophic wildfire: The Black Saturday Kilmore
996 East fire in Victoria, Australia, Forest Ecol. Manag. 284 (2012) 269–285.

- 997 [17] R. Paugam, M. Wooster, S. Freitas, M. Val Martin, A review of ap-
 998 proaches to estimate wildfire plume injection height within large-scale
 999 atmospheric chemical transport models, *Atmos. Chem. Phys.* 16 (2)
 1000 (2016) 907–925. doi:10.5194/acp-16-907-2016.
- 1001 [18] E. Koo, P. J. Pagni, D. R. Weise, J. P. Woycheese, Firebrands and
 1002 spotting ignition in large-scale fires, *Int. J. Wildland Fire* 19 (7) (2010)
 1003 818–843.
 1004 URL <https://doi.org/10.1071/WF07119>
- 1005 [19] M. Finney, FARSITE: Fire Area Simulator - Model Development and
 1006 Evaluation, Tech. Rep. February, US Department of Agriculture, Forest
 1007 Service, Rocky Mountain Research Station (1998).
- 1008 [20] J.-B. Filippi, F. Bosseur, C. Mari, C. Lac, P. Le Moigne, B. Cuenot,
 1009 D. Veynante, D. Cariolle, J.-H. Balbi, Coupled atmosphere-wildland fire
 1010 modelling, *J. Adv. Model. Earth Sy.* 1 (4) (2009) Quarter 4.
- 1011 [21] C. Tymstra, R. W. Bryce, B. M. Wotton, S. W. Taylor, O. B. Armitage,
 1012 Development and structure of Prometheus: the Canadian Wildland Fire
 1013 Growth Simulation Model, Tech. rep., Natural Resources Canada, Cana-
 1014 dian Forest Service, Northern Forestry Centre, Edmonton, Alberta, In-
 1015 formation Report NOR-X-417 (2010).
- 1016 [22] D. Chong, K. G. Tolhurst, T. J. Duff, B. Cirulis, Sensitivity Analysis
 1017 of PHOENIX RapidFire, Tech. rep., Bushfire CRC, University of Mel-
 1018 bourne (2013).

- 1019 [23] C. Lautenberger, Wildland fire modeling with an eulerian level set
1020 method and automated calibration, *Fire Safety J.* 62, Part C (2013) 289
1021 – 298. doi:<http://dx.doi.org/10.1016/j.firesaf.2013.08.014>.
- 1022 [24] A. Sullivan, Wildland surface fire spread modeling, 1990-2007. 2: Empir-
1023 ical and quasi-empirical models, *Int. J. Wildland Fire* 18 (2009) 369–386.
- 1024 [25] M. Gollner, A. Trouvé, I. Altintas, J. Block, R. De Callafon,
1025 C. Clements, A. Cortes, E. Ellicott, J.-B. Filippi, M. Finney, K. Ide, M.-
1026 A. Jenkins, D. Jimenez, C. Lautenberger, J. Mandel, M. C. Rochoux,
1027 A. Simeoni, Towards data-driven operational wildfire spread modeling -
1028 report of the nsf-funded wfire workshop, Tech. rep., University of Mary-
1029 land (2015).
- 1030 [26] M. G. Cruz, M. E. Alexander, Limitations of the accuracy of model pre-
1031 dictions of wildland fire behaviour: A state-of-the-knowledge overview,
1032 *The Forestry Chronicle* 89 (3) (2013) 372–383. doi:[https://doi.org/](https://doi.org/10.5558/tfc2013-067)
1033 [10.5558/tfc2013-067](https://doi.org/10.5558/tfc2013-067).
- 1034 [27] M. G. Cruz, M. E. Alexander, A. L. Sullivan, J. S. Gould, M. Kilinc, As-
1035 sessing improvements in models used to operationally predict wildland
1036 fire rate of spread, *Environmental Modelling & Software* 105 (2018) 54
1037 – 63. doi:<https://doi.org/10.1016/j.envsoft.2018.03.027>.
1038 URL [http://www.sciencedirect.com/science/article/pii/](http://www.sciencedirect.com/science/article/pii/S1364815218300161)
1039 [S1364815218300161](http://www.sciencedirect.com/science/article/pii/S1364815218300161)
- 1040 [28] E. Jimenez, M. Hussaini, S. Goodrick, Quantifying parametric uncer-
1041 tainty in the Rothermel model, *Int. J. Wildland Fire* 17 (2008) 638–649.

- 1042 [29] Y. Liu, M. Y. Hussaini, G. Oktenb, Global sensitivity analysis for the
1043 rothermel model based on high-dimensional model representation, Cana-
1044 dian Journal of Forest Research 45 (11) (2015) 1474–1479. doi:<https://doi.org/10.1139/cjfr-2015-0148>.
1045
- 1046 [30] M. Denham, K. Wendt, G. Bianchini, A. Cortés, T. Margalef, Dynamic
1047 data-driven genetic algorithm for forest fire spread prediction, J. Com-
1048 put. Sci-Neth. 3 (2012) 398–404.
- 1049 [31] M. C. Rochoux, B. Delmotte, B. Cuenot, S. Ricci, A. Trouvé, Regional-
1050 scale simulations of wildland fire spread informed by real-time flame
1051 front observations, P. Combust. Inst. 34 (2013) 2641–2647. doi:10.
1052 1016/j.proci.2012.06.090.
- 1053 [32] M. C. Rochoux, S. Ricci, B. Lucor, D. and Cuenot, A. Trouvé, Towards
1054 predictive data-driven simulations of wildfire spread - Part 1: Reduced-
1055 cost Ensemble Kalman Filter based on a Polynomial Chaos surrogate
1056 model for parameter estimation, Nat. Hazards and Earth Syst. Sci.
1057 14 (11) (2014) 2951–2973.
- 1058 [33] T. Artes, A. Cencerrado, A. Cortes, T. Margalef, D. Rodriguez-Aseretto,
1059 T. Petroliagkis, J. San-Miguel-Ayanz, Towards a dynamic data driven
1060 wildfire behavior prediction system at european level, Procedia Com-
1061 puter Science 29 (2014) 1216 – 1226. doi:[http://dx.doi.org/10.](http://dx.doi.org/10.1016/j.procs.2014.05.109)
1062 1016/j.procs.2014.05.109.
- 1063 [34] M. C. Rochoux, C. Emery, S. Ricci, B. Cuenot, A. Trouvé, Towards
1064 predictive data-driven simulations of wildfire spread – part ii: Ensemble

- 1065 kalman filter for the state estimation of a front-tracking simulator of
 1066 wildfire spread, *Nat. Hazards and Earth Syst. Sci.* 15 (8) (2015) 1721–
 1067 1739. doi:[10.5194/nhess-15-1721-2015](https://doi.org/10.5194/nhess-15-1721-2015).
- 1068 [35] C. Zhang, M. C. Rochoux, W. Tang, M. Gollner, J. B. Filippi, A. Trouvé,
 1069 Evaluation of a data-driven wildland fire spread forecast model with
 1070 spatially-distributed parameter estimation in simulations of the fireflux
 1071 i field-scale experiment, *Fire Safety J.* 91 (2017) 758 – 767, *fire Safety*
 1072 *Science: Proceedings of the 12th International Symposium*. doi:[http:](http://dx.doi.org/10.1016/j.firesaf.2017.03.057)
 1073 [//dx.doi.org/10.1016/j.firesaf.2017.03.057](http://dx.doi.org/10.1016/j.firesaf.2017.03.057).
- 1074 [36] M. C. Rochoux, A. Collin, C. Zhang, A. Trouvé, D. Lucor, P. Moireau,
 1075 Front shape similarity measure for shape-oriented sensitivity analysis
 1076 and data assimilation for Eikonal equation, *ESAIM: Proceedings and*
 1077 *Surveys* 63 (2018) 215–236.
 1078 URL <https://hal.inria.fr/hal-01625575>
- 1079 [37] S. L. Manzello, T. G. Cleary, J. R. Shields, A. Maranghides, W. Mell,
 1080 J. C. Yang, Experimental investigation of firebrands: Generation and
 1081 ignition of fuel beds, *Fire Safety J.* 43 (3) (2008) 226 – 233. doi:[https:](https://doi.org/10.1016/j.firesaf.2006.06.010)
 1082 [//doi.org/10.1016/j.firesaf.2006.06.010](https://doi.org/10.1016/j.firesaf.2006.06.010).
- 1083 [38] N. Sardoy, J. Consalvi, A. Kaiss, A. Fernandez-Pello, B. Porterie,
 1084 Numerical study of ground-level distribution of firebrands gen-
 1085 erated by line fires, *Combust. Flame* 154 (3) (2008) 478 – 488.
 1086 doi:<https://doi.org/10.1016/j.combustflame.2008.05.006>.
 1087 URL [http://www.sciencedirect.com/science/article/pii/](http://www.sciencedirect.com/science/article/pii/S0010218008001600)
 1088 [S0010218008001600](http://www.sciencedirect.com/science/article/pii/S0010218008001600)

- 1089 [39] S. Kortas, P. Mindykowski, J. L. Consalvi, H. Mhiri, B. Porterie, Exper-
1090 imental validation of a numerical model for the transport of firebrands,
1091 Fire Safety J. 44 (2009) 1095–1102.
- 1092 [40] H. A. Perryman, A mathematical model of spot fires and their manage-
1093 ment implications, Master’s thesis, Humboldt State University, Arcata,
1094 CA (2009).
- 1095 [41] H. A. Perryman, C. J. Dugaw, J. M. Varner, D. L. Johnson, A cellular
1096 automata model to link surface fires to firebrand lift-off and dispersal,
1097 Int. J. Wildland Fire 22 (2013) 428–439.
- 1098 [42] A. Tohidi, N. Kaye, W. Bridges, Statistical description of firebrand size
1099 and shape distribution from coniferous trees for use in metropolis monte
1100 carlo simulations of firebrand flight distance, Fire Safety J. 77 (2015)
1101 21 – 35. doi:<https://doi.org/10.1016/j.firesaf.2015.07.008>.
1102 URL [http://www.sciencedirect.com/science/article/pii/](http://www.sciencedirect.com/science/article/pii/S0379711215300047)
1103 [S0379711215300047](http://www.sciencedirect.com/science/article/pii/S0379711215300047)
- 1104 [43] A. Tohidi, Experimental and numerical modeling of wildfire spread via
1105 fire spotting, Ph.D. thesis, Clemson University, South Carolina, USA
1106 (2016).
- 1107 [44] A. Tohidi, N. B. Kaye, Stochastic modeling of firebrand shower
1108 scenarios, Fire Safety J. 91 (2017) 91 – 102, fire Safety Sci-
1109 ence: Proceedings of the 12th International Symposium.
1110 doi:<https://doi.org/10.1016/j.firesaf.2017.04.039>.

- 1111 URL [http://www.sciencedirect.com/science/article/pii/](http://www.sciencedirect.com/science/article/pii/S0379711217302461)
1112 [S0379711217302461](http://www.sciencedirect.com/science/article/pii/S0379711217302461)
- 1113 [45] G. Pagnini, L. Massidda, Modelling turbulence effects in wildland
1114 fire propagation by the randomized level-set method, Tech. Rep
1115 2012/PM12a, CRS4, revised Version August 2014. arXiv:1408.6129
1116 (July 2012).
- 1117 [46] G. Pagnini, Fire spotting effects in wildland fire propagation, in:
1118 F. Casas, V. Martínez (Eds.), Advances in Differential Equations and
1119 Applications, Vol. 4 of SEMA SIMAI Springer Series, Springer Inter-
1120 national Publishing Switzerland, 2014, pp. 203–216, iISBN: 978-3-319-
1121 06952-4. (eBook: 978-3-319-06953-1).
- 1122 [47] G. Pagnini, A. Mentrelli, Modelling wildland fire propagation by track-
1123 ing random fronts, Nat. Hazards Earth Syst. Sci. 14 (2014) 2249–2263.
- 1124 [48] I. Kaur, A. Mentrelli, F. Bosseur, J.-B. Filippi, G. Pagnini, Tur-
1125 bulence and fire-spotting effects into wild-land fire simulators, Com-
1126 mun. Nonlinear Sci. Numer. Simul. 39 (2016) 300 – 320. doi:<http://doi.org/10.1016/j.cnsns.2016.03.003>.
1127
- 1128 [49] A. Saltelli, M. Ratto, T. Andres, F. Campolongo, J. Cariboni, D. Gatelli,
1129 M. Saisana, S. Tarantola, Global Sensitivity Analysis. The Primer,
1130 John Wiley & Sons, Ltd, Chichester, UK, 2007. doi:[10.1002/](https://doi.org/10.1002/9780470725184)
1131 [9780470725184](https://doi.org/10.1002/9780470725184).
- 1132 [50] C. Storlie, L. Swiler, J. Helton, C. Sallaberry, Implementation and eval-
1133 uation of nonparametric regression procedures for sensitivity analysis

- 1134 of computationally demanding models, Reliab. Eng. Syst. Safe. 94 (11)
1135 (2009) 1735–1763. doi:10.1016/j.ress.2009.05.007.
- 1136 [51] M. Lamboni, H. Monod, D. Makowski, Multivariate sensitivity analy-
1137 sis to measure global contribution of input factors in dynamic models,
1138 Reliab. Eng. Syst. Safe. 96 (4) (2011) 450–459. doi:10.1016/j.ress.
1139 2010.12.002.
- 1140 [52] J. J. Ruiz, M. Pulido, T. Miyoshi, Estimating model parameters with
1141 ensemble-based data assimilation: A review, Journal of the Meteorolog-
1142 ical Society of Japan. Ser. II 91 (2) (2013) 79–99. doi:10.2151/jmsj.
1143 2013-201.
- 1144 [53] I. Sobol, Sensitivity analysis for nonlinear mathematical models, Mathe-
1145 matical Modeling and Computational Experiment 1 (4) (1993) 407–414.
- 1146 [54] B. Sudret, Global sensitivity analysis using polynomial chaos expan-
1147 sions, Reliab. Eng. Syst. Safe. 93 (7) (2008) 964–979. doi:10.1016/j.
1148 ress.2007.04.002.
- 1149 [55] A. Marrel, B. Iooss, B. Laurent, O. Roustant, Calculations of sobol
1150 indices for the gaussian process metamodel, Reliab. Eng. Syst. Safe.
1151 94 (3) (2009) 742 – 751. doi:http://dx.doi.org/10.1016/j.ress.
1152 2008.07.008.
- 1153 [56] B. Iooss, A. Saltelli, Introduction to Sensitivity Analysis, in: Handbook
1154 of Uncertainty Quantification, Springer International Publishing, 2016,
1155 pp. 1–20. doi:10.1007/978-3-319-11259-6_31-1.

- 1156 [57] L. Le Gratiet, S. Marelli, B. Sudret, Metamodel-Based Sensitivity Anal-
 1157 ysis: Polynomial Chaos Expansions and Gaussian Processes, in: Hand-
 1158 book of Uncertainty Quantification, Springer International Publishing,
 1159 2017, pp. 1–37. doi:10.1007/978-3-319-11259-6_38-1.
- 1160 [58] N. Owen, P. Challenor, P. P. Menon, S. Bennani, Comparison of
 1161 surrogate-based uncertainty quantification methods for computationally
 1162 expensive simulators, SIAM/ASA Journal on Uncertainty Quantifica-
 1163 tion 5 (1) (2017) 403–435. doi:10.1137/15M1046812.
- 1164 [59] V. Ciriello, V. Di Federico, M. Riva, F. Cadini, J. De Sanctis, E. Zio,
 1165 A. Guadagnini, Polynomial chaos expansion for global sensitivity anal-
 1166 ysis applied to a model of radionuclide migration in a randomly hetero-
 1167 geneous aquifer, Stoch. Env. Res. Risk A. 27 (4) (2013) 945–954.
- 1168 [60] B. Després, G. Poette, D. Lucor, Robust Uncertainty Propagation
 1169 in Systems of Conservation Laws with the Entropy Closure Method,
 1170 Springer International Publishing, 2013, pp. 105–149. doi:10.1007/
 1171 978-3-319-00885-1_3.
- 1172 [61] S. Dubreuil, M. Berveiller, F. Petitjean, M. Salan, Construction of
 1173 bootstrap confidence intervals on sensitivity indices computed by poly-
 1174 nomial chaos expansion, Reliab. Eng. Syst. Safe. 121 (2014) 263–275.
 1175 doi:10.1016/j.ress.2013.09.011.
- 1176 [62] D. Xiu, Numerical Methods for Stochastic Computations: A Spectral
 1177 Method Approach, Princeton University Press, 2010.

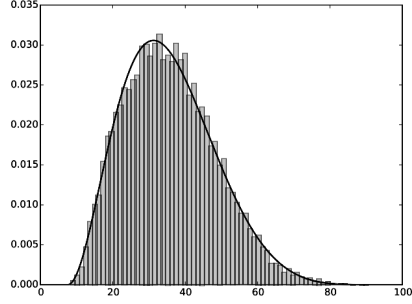
- 1178 [63] M. De Lozzo, A. Marrel, Sensitivity analysis with dependence and
1179 variance-based measures for spatio-temporal numerical simulators,
1180 Stoch. Env. Res. Risk A. 31 (6) (2017) 1437–1453.
- 1181 [64] L. Le Gratiet, C. Cannamela, B. Iooss, A bayesian approach for global
1182 sensitivity analysis of (multifidelity) computer codes, SIAM/ASA Jour-
1183 nal on Uncertainty Quantification 2 (1) (2014) 336–363. doi:10.1137/
1184 130926869.
- 1185 [65] A. Marrel, G. Perot, C. Mottet, Development of a surrogate model
1186 and sensitivity analysis for spatio-temporal numerical simulators, Stoch.
1187 Env. Res. Risk A. 29 (3) (2015) 959–974.
- 1188 [66] J. Oakley, A. O’Hagan, Probabilistic sensitivity analysis of complex
1189 models: a bayesian approach, J. Roy. Stat. Soc. B 66 (3) (2004) 751–769.
1190 doi:10.1111/j.1467-9868.2004.05304.x.
- 1191 [67] C. Rasmussen, C. Williams, Gaussian processes for machine learning,
1192 MIT Press, 2006.
- 1193 [68] P. T. Roy, N. El Moçayd, S. Ricci, J.-C. Jouhaud, N. Goutal,
1194 M. De Lozzo, M. C. Rochoux, Comparison of polynomial chaos and
1195 gaussian process surrogates for uncertainty quantification and corre-
1196 lation estimation of spatially distributed open-channel steady flows,
1197 Stoch. Env. Res. Risk A. 32 (6) (2018) 1723–1741. doi:10.1007/
1198 s00477-017-1470-4.
1199 URL <https://doi.org/10.1007/s00477-017-1470-4>

- 1200 [69] R. Schoebi, B. Sudret, J. Wiart, Polynomial-Chaos-based Kriging, Int.
1201 J. Uncertain. Quan. 5 (2) (2015) 171–193.
- 1202 [70] G. Blatman, Adaptative sparse Polynomial Chaos expansions for un-
1203 certainty propagation and sensitivity analysis, Ph.D. thesis, Université
1204 Blaise Pascal, Clermont-Ferrand (2009).
- 1205 [71] G. Blatman, B. Sudret, Adaptative sparse polynomial chaos expansion
1206 based on Least Angle Regression, J. Comput. Phys. 230 (6) (2011) 2345–
1207 2367.
- 1208 [72] G. Migliorati, F. Nobile, E. Von Schwerin, R. Tempone, Approximation
1209 of quantities of interest in stochastic PDEs by the random Discret L2
1210 Projection on polynomial spaces, SIAM J. Sci Comput. 35 (3) (2013)
1211 A1440–A1460.
- 1212 [73] J. Sethian, Level set methods and fast marching methods, Cambridge
1213 University Press, 1999.
- 1214 [74] S. Osher, R. Fedkiw, Level set methods and dynamic implicit surfaces,
1215 Vol. 153, Applied Mathematical Sciences - Springer, 2003.
- 1216 [75] V. Mallet, D. Keyes, F. Fendell, Modeling wildland fire propagation
1217 with level set methods, Comput. Math. Appl. 57 (7) (2009) 1089–1101.
1218 doi:10.1016/J.CAMWA.2008.10.089.
- 1219 [76] C. Lautenberger, Mapping areas at elevated risk of large-scale structure
1220 loss using monte carlo simulation and wildland fire modeling, Fire Safety

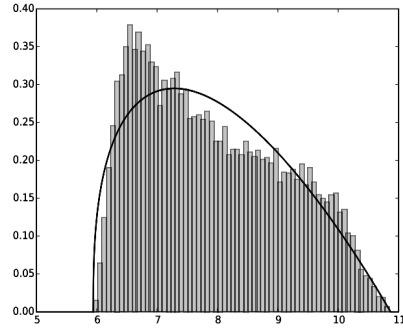
- 1221 J. 91 (2017) 768 – 775, fire Safety Science: Proceedings of the 12th In-
 1222 ternational Symposium. doi:[https://doi.org/10.1016/j.firesaf.](https://doi.org/10.1016/j.firesaf.2017.04.014)
 1223 2017.04.014.
- 1224 [77] A. Mentrelli, G. Pagnini, Front propagation in anomalous diffusive me-
 1225 dia governed by time-fractional diffusion, J. Comput. Phys. 293 (2015)
 1226 427–441.
- 1227 [78] G. M. Byram, Combustion of forest fuels, in: K. P. Davis (Ed.), Forest
 1228 Fire: Control and Use, McGraw Hill, New York, 1959, pp. 61–89.
- 1229 [79] M. E. Alexander, Calculating and interpreting forest fire intensities,
 1230 Can. J. Bot. 60 (1982) 349–357.
- 1231 [80] M. Sofiev, T. Ermakova, R. Vankevich, Evaluation of the smoke-
 1232 injection height from wild-land fires using remote-sensing data,
 1233 Atmos. Chem. Phys. 12 (4) (2012) 1995–2006. doi:10.5194/
 1234 acp-12-1995-2012.
 1235 URL <https://www.atmos-chem-phys.net/12/1995/2012/>
- 1236 [81] D. Xiu, G. Karniadakis, The wiener–askey polynomial chaos for stochas-
 1237 tic differential equations, SIAM J. Sci. Comput. 24 (2) (2002) 619–644.
 1238 doi:10.1137/S1064827501387826.
- 1239 [82] E. Jones, T. Oliphant, P. Peterson, et al., SciPy: Open source scientific
 1240 tools for Python, [Online; accessed on 06/02/2019] (2001–).
 1241 URL <http://www.scipy.org/>
- 1242 [83] K. T. Chu, M. Prodanović, Level set method library (lsmlib), Tech. rep.,

- 1243 accessed 16th August 2018 (2009).
 1244 URL <http://ktchu.serendipityresearch.org/software/lsmllib/>
- 1245 [84] C. D. Bevins, Firelib: User manual and technical reference, Tech. rep.,
 1246 US Forest Service, Missoula Fire Sciences Laboratory, Fire Behavior
 1247 Research Work Unit Systems for Environmental Management, accessed
 1248 16th August 2018 (1996).
 1249 URL <https://www.frames.gov/catalog/935>
- 1250 [85] M. Baudin, A. Dutfoy, B. Iooss, A.-L. Popelin, OpenTURNS: An
 1251 Industrial Software for Uncertainty Quantification in Simulation,
 1252 Springer International Publishing, 2017, pp. 2001–2038. doi:10.1007/
 1253 978-3-319-12385-1-64.
 1254 URL <https://doi.org/10.1007/978-3-319-12385-1-64>
- 1255 [86] B. Efron, T. Hastie, I. Johnstone, R. Tibshirani, Least angle re-
 1256 gression, *Ann. Statist.* 32 (2) (2004) 407–499. doi:10.1214/
 1257 0090536040000000067.
 1258 URL <https://doi.org/10.1214/0090536040000000067>
- 1259 [87] D. J. Wales, J. P. K. Doye, Global Optimization by Basin-Hopping and
 1260 the Lowest Energy Structures of Lennard-Jones Clusters Containing up
 1261 to 110 Atoms, *The Journal of Physical Chemistry A* 101 (28) (1997)
 1262 5111–5116. doi:10.1021/jp970984n.
- 1263 [88] M. Baudin, K. Boumhaout, T. Delage, B. Iooss, J.-M. Martinez, Numer-
 1264 ical stability of Sobol’ indices estimation formula, in: 8th International

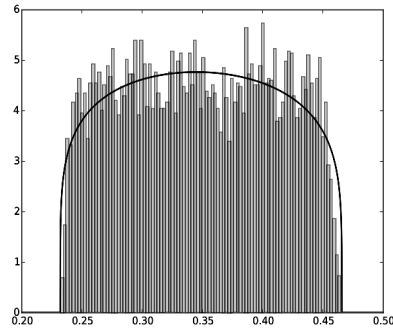
- 1265 Conference on Sensitivity Analysis of Model Output,, Réunion Island,
1266 2016.
- 1267 [89] F. Pedregosa, G. Varoquaux, A. Gramfort, V. Michel, B. Thirion,
1268 O. Grisel, M. Blondel, P. Prettenhofer, R. Weiss, V. Dubourg, J. Van-
1269 derplas, A. Passos, D. Cournapeau, M. Brucher, M. Perrot, É. Duch-
1270 esnay, Scikit-learn: Machine Learning in Python, J. Mach. Learn. Res.
1271 12 (2825-2830). [arXiv:1201.0490](https://arxiv.org/abs/1201.0490).
- 1272 [90] P. T. Roy, S. Ricci, R. Dupuis, R. Campet, J.-C. Jouhaud, C. Fournier,
1273 Batman: Statistical analysis for expensive computer codes made easy,
1274 Journal of Open Source Software 3 (21) (2018) 493. [doi:https://doi.](https://doi.org/10.21105/joss.00493)
1275 [org/10.21105/joss.00493](https://doi.org/10.21105/joss.00493).
- 1276 [91] S. W. Taylor, D. G. Woolford, C. B. Dean, D. L. Martell, Wildfire
1277 prediction to inform fire management: Statistical science challenges,
1278 Stat. Sci. 28 (2013) 586–615.
- 1279 [92] J. San-Miguel-Ayanz, J. M. Moreno, A. Camia, Analysis of large fires in
1280 European Mediterranean landscapes: lessons learned and perspectives,
1281 Forest Ecol. Manage. 294 (2013) 11–22.
- 1282 [93] C. Hernandez, C. Keribin, P. Drobinski, S. Turquety, Statistical mod-
1283 elling of wildfire size and intensity: a step toward meteorological fore-
1284 casting of summer extreme fire risk, Ann. Geophys. 33 (2015) 1495–1506.



(a) Fire-spotting parameter μ .



(b) Fire-spotting parameter σ .



(c) Turbulent diffusion parameter D [$\text{m}^2 \text{s}^{-1}$].

Figure 1: Histograms and corresponding fits with Beta-distribution (solid lines) for the three parameters μ , σ (fire-spotting effects) and D (turbulence effect) following a Monte Carlo random sampling with 10,000 realizations in the ensemble. Fits performed with the aid of the Python library SciPy [82].

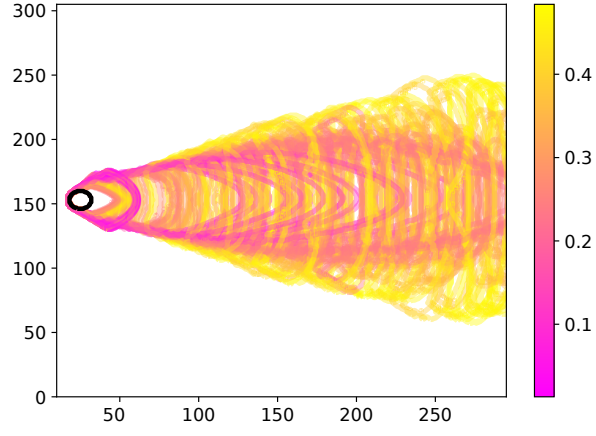


Figure 2: Ensemble of 100 fireline positions over the 2-D computational domain Ω after 50 min of **LSFire+** model integration obtained when varying D , μ and σ as presented in Table 5. The black circle is the initial fireline that is the same for all simulations. The colormap corresponds to the normalized MSR S_t at time $t = 50$ min (Eq. 15).

Table 7: Types of surrogate used in this work. Recall that q is the hyperbolic parameter for truncation ($q = 1$ corresponds to linear truncation) and N is the size of the training set.

Name	Truncation	Sparse	Training set
Quad. (Quadrature)	$q = 1, 0.75, 0.5$	No	Gauss quadrature, $N = 216$
SLS (Standard Least-Squares)	$q = 1, 0.75, 0.5$	No	Halton, $N = 216$
LAR (Least-Angle Regression)	$q = 1, 0.75, 0.5$	Yes	Halton, $N = 216$
Cleaning	$q = 1, 0.75, 0.5$	Yes	Halton, $N = 216$
Sequential	$q = 1, 0.75, 0.5$	Yes	Halton, $N = 216$
RBF kernel	–	–	Halton, $N = 216$

Table 8: Error metrics ϵ_{emp} and Q_2 for gPC-expansions and GP-model detailed in Table 7. The size of the training set is $N = 216$. One type of surrogate is built for each of the four observables, A_1 , A_2 , S_1 and S_2 .

	gPC expansion – Linear truncation ($q = 1$)							
	A_1		A_2		S_1		S_2	
	ϵ_{emp}	Q_2	ϵ_{emp}	Q_2	ϵ_{emp}	Q_2	ϵ_{emp}	Q_2
Quad.	$1.4 \cdot 10^{-4}$	0.84	$2.7 \cdot 10^{-4}$	0.86	$5.5 \cdot 10^{-4}$	0.77	$4.6 \cdot 10^{-4}$	0.83
SLS	$3.0 \cdot 10^{-4}$	0.83	$6.3 \cdot 10^{-4}$	0.88	$1.0 \cdot 10^{-3}$	0.74	$2.3 \cdot 10^{-3}$	0.75
LAR	$1.0 \cdot 10^{-4}$	0.99	$4.2 \cdot 10^{-4}$	0.970	$5.0 \cdot 10^{-4}$	0.96	$2.3 \cdot 10^{-3}$	0.95
Cleaning	$1.0 \cdot 10^{-4}$	0.96	$4.1 \cdot 10^{-4}$	0.95	$5.5 \cdot 10^{-4}$	0.96	$1.2 \cdot 10^{-3}$	0.95
Sequential	$3.3 \cdot 10^{-4}$	0.85	$6.7 \cdot 10^{-4}$	0.89	$1.1 \cdot 10^{-3}$	0.77	$2.5 \cdot 10^{-3}$	0.85
	gPC expansion – Hyperbolic truncation ($q = 0.75$)							
	A_1		A_2		S_1		S_2	
	ϵ_{emp}	Q_2	ϵ_{emp}	Q_2	ϵ_{emp}	Q_2	ϵ_{emp}	Q_2
Quad.	$3.7 \cdot 10^{-4}$	0.76	$8.6 \cdot 10^{-4}$	0.77	$1.6 \cdot 10^{-3}$	0.67	$3.7 \cdot 10^{-4}$	0.66
SLS	$1.5 \cdot 10^{-4}$	0.93	$1.8 \cdot 10^{-4}$	0.93	$1.0 \cdot 10^{-3}$	0.84	$2.5 \cdot 10^{-3}$	0.84
LAR	$2.0 \cdot 10^{-4}$	0.94	$5.6 \cdot 10^{-4}$	0.95	$1.0 \cdot 10^{-3}$	0.84	$2.6 \cdot 10^{-3}$	0.86
Cleaning	$9.9 \cdot 10^{-5}$	0.94	$3.3 \cdot 10^{-4}$	0.90	$5.0 \cdot 10^{-4}$	0.96	$1.1 \cdot 10^{-3}$	0.96
Sequential	$1.9 \cdot 10^{-4}$	0.94	$4.7 \cdot 10^{-4}$	0.94	$8.7 \cdot 10^{-4}$	0.86	$1.9 \cdot 10^{-3}$	0.92
	gPC expansion – Hyperbolic truncation ($q = 0.5$)							
	A_1		A_2		S_1		S_2	
	ϵ_{emp}	Q_2	ϵ_{emp}	Q_2	ϵ_{emp}	Q_2	ϵ_{emp}	Q_2
Quad.	$1.8 \cdot 10^{-4}$	0.83	$2.0 \cdot 10^{-4}$	0.87	$6.2 \cdot 10^{-4}$	0.74	$3.6 \cdot 10^{-4}$	0.83
SLS	$1.4 \cdot 10^{-4}$	0.96	$9.6 \cdot 10^{-5}$	0.95	$7.4 \cdot 10^{-4}$	0.86	$1.9 \cdot 10^{-3}$	0.86
LAR	$1.5 \cdot 10^{-4}$	0.97	$4.3 \cdot 10^{-4}$	0.97	$6.5 \cdot 10^{-4}$	0.93	$1.6 \cdot 10^{-3}$	0.94
Cleaning	$8.8 \cdot 10^{-5}$	0.95	$3.3 \cdot 10^{-4}$	0.94	$4.5 \cdot 10^{-4}$	0.92	$9.2 \cdot 10^{-4}$	0.98
Sequential	$1.3 \cdot 10^{-4}$	0.97	$4.2 \cdot 10^{-4}$	0.96	$6.4 \cdot 10^{-4}$	0.93	$1.5 \cdot 10^{-3}$	0.95
GP model								
RBF	—	0.99	—	0.98	—	0.88	—	0.99

Figure 3: Comparison between quadrature, SLS and sparse (LAR, cleaning, sequential) methods to build the gPC-expansion for the burnt area ratio A_2 using linear truncation. Left: sparsity plots representing the magnitude of the coefficients with respect to the three-dimensional input space ($d = 3$). Right: adequacy scatter plots comparing surrogate (x -axis) and model (y -axis) predictions at the training points. For SLS and LAR, results are obtained with the best fit obtained for varying P .

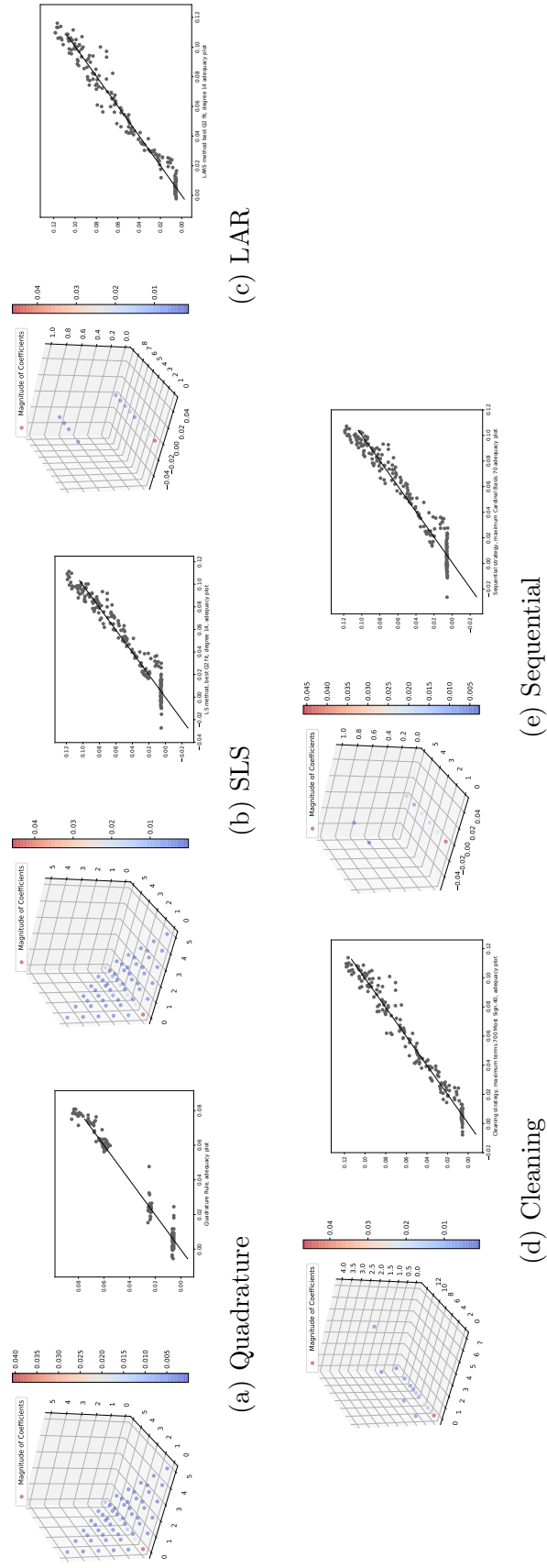
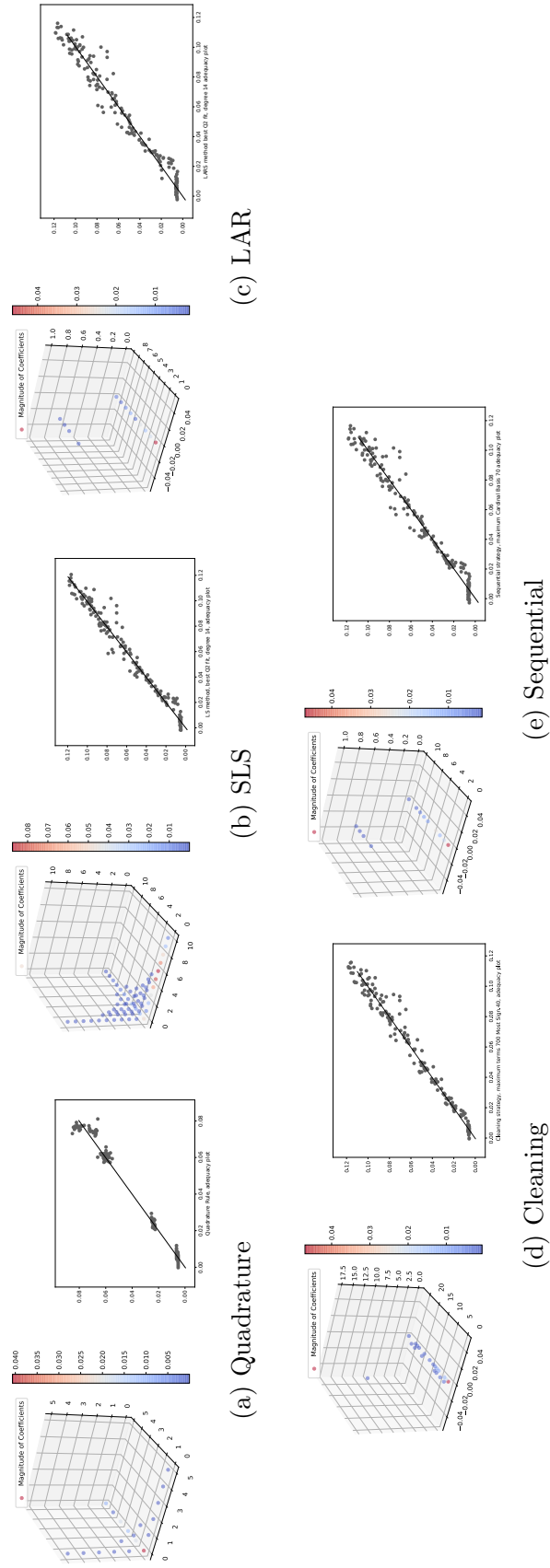


Figure 4: Comparison between quadrature, SLS and sparse (LAR, cleaning, sequential) methods to build the gPC-expansion for the burnt area ratio A_2 using linear truncation. Left: sparsity plots representing the magnitude of the coefficients with respect to the three-dimensional input space ($d = 3$). Right: adequacy scatter plots comparing surrogate (x -axis) and model (y -axis) predictions at the training points. For SLS and LAR, results are obtained with the best fit obtained for varying P .



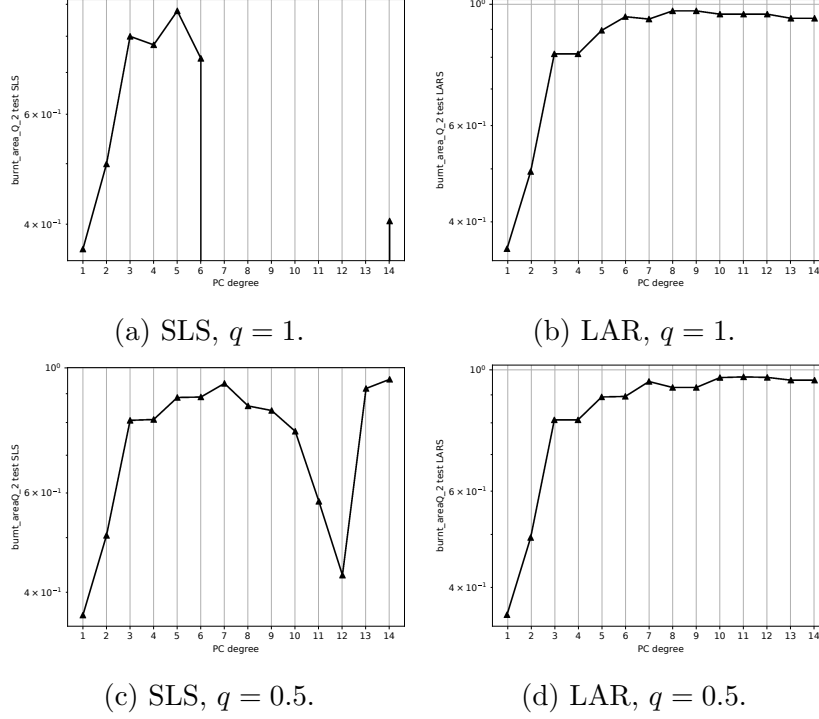


Figure 5: Sensitivity of the Q_2 predictive coefficient with respect to the total polynomial order P . Comparison of the SLS (a)–(c) and LAR (b)–(d) surrogate methods for linear truncation (top panels) and hyperbolic truncation with $q = 0.5$ (bottom panels) for $1 \leq P \leq 14$.

Table 9: Comparison of Sobol’ sensitivity indices associated with the burnt area ratio A_2 and obtained for Halton’s low discrepancy sequence.

	S_μ	S_σ	S_D	$S_{T,\mu}$	$S_{T,\sigma}$	$S_{T,D}$
gPC expansion – Linear truncation $q = 1$						
LAR	0.	0.986	$5.67 \cdot 10^{-3}$	0.	0.994	$1.35 \cdot 10^{-2}$
Cleaning	0.	0.984	$5.89 \cdot 10^{-3}$	$4.70 \cdot 10^{-3}$	0.994	$1.62 \cdot 10^{-2}$
Sequential	0.	0.987	$4.84 \cdot 10^{-3}$	0.	0.995	$1.33 \cdot 10^{-2}$
GP model						
RBF kernel	$4.59 \cdot 10^{-4}$	0.982	$5.97 \cdot 10^{-3}$	0.001	0.992	0.012

Table 10: Same caption as Table 9 but for the MSR ratio S_2 .

	S_μ	S_σ	S_D	$S_{T,\mu}$	$S_{T,\sigma}$	$S_{T,D}$
	gPC expansion – Linear truncation $q = 1$					
LAR	0.	0.948	$1.49 \cdot 10^{-2}$	0.	0.985	$5.22 \cdot 10^{-2}$
Cleaning	0.	0.925	$1.66 \cdot 10^{-2}$	$2.66 \cdot 10^{-3}$	0.983	$7.18 \cdot 10^{-2}$
Sequential	0.	0.954	$1.45 \cdot 10^{-2}$	$7.15 \cdot 10^{-3}$	0.978	$4.63 \cdot 10^{-2}$
	GP model					
RBF kernel	$5.43 \cdot 10^{-4}$	0.941	$9.89 \cdot 10^{-3}$	0.002	0.975	0.047

Table 11: Mean and STD estimate of the burnt area ratio A_2 (left column) and of the MSR ratio S_2 (right column) using linear truncation scheme ($q = 1$), Halton’s low discrepancy sequence and gPC or GP surrogate approach.

	A_2	S_2
	gPC expansion – Linear truncation ($q = 1$)	
	mean \pm STD	mean \pm STD
Quad.	0.0406 ± 0.175	0.102 ± 0.322
SLS	0.0458 ± 0.198	0.114 ± 0.333
LAR	0.0464 ± 0.194	0.114 ± 0.324
Cleaning	0.0469 ± 0.194	0.115 ± 0.327
Sequential	0.0458 ± 0.196	0.113 ± 0.319
	GP model	
	mean \pm STD	mean \pm STD
RBF kernel	0.0463 ± 0.194	0.114 ± 0.327

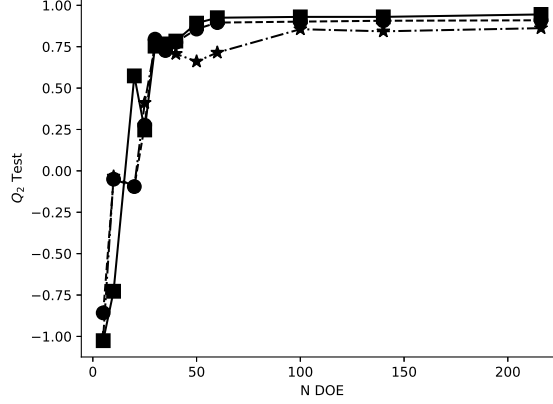


Figure 6: Convergence test with respect to Q_2 predictive coefficient for the LAR gPC-surrogate built using Halton's low discrepancy sequence (cross-validated using the Monte Carlo random sampling). Solid line with square symbols corresponds to linear truncation; dash-dotted line with star symbols corresponds to hyperbolic truncation with $q = 0.75$; and dashed line with circle symbols corresponds to hyperbolic truncation with $q = 0.5$.

Table 12: Sobol' indices (first-order in black and total-order in gray) using LAR gPC-surrogate and linear truncation; $\theta = (U, I, \tau)^T$; $N = 216$. Left: Sobol' indices associated with the burnt area ratio A_2 . Right: Sobol' indices associated with the MSR ratio S_2 .

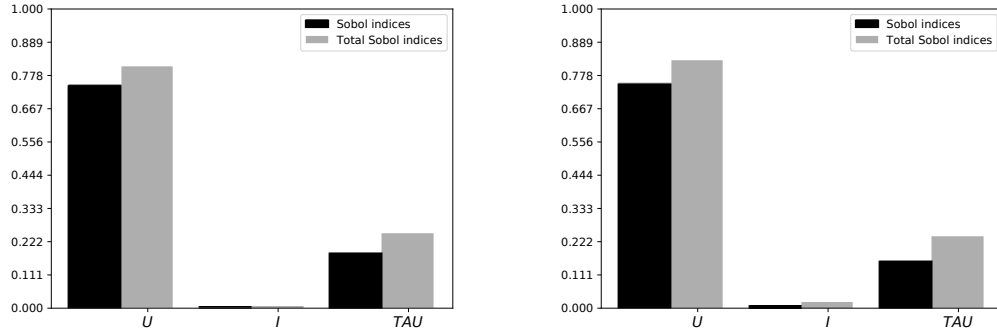


Table 13: Mean and STD of observables A_2 and S_2 as well as error metrics ϵ_{emp} and Q_2 using LAR gPC-surrogate and linear truncation; $\theta = (U, I, \tau)^T$; $N = 216$.

Quantity of interest	Mean	STD	ϵ_{emp}	Q_2
A_2	0.07	0.06	$9 \cdot 10^{-4}$	0.95
S_2	0.19	0.13	$2 \cdot 10^{-3}$	0.96

Table 14: Same caption as in Table 12 but for $\theta = (\mu, \sigma, D)^T$.

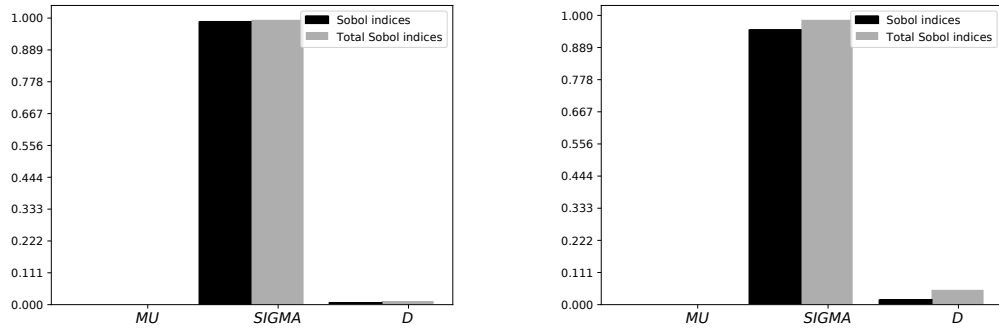


Table 15: Same caption as in Table 13 but for $\theta = (\mu, \sigma, D)^T$.

Quantity of interest	Mean	STD	ϵ_{emp}	Q_2
A_2	0.05	0.04	$4 \cdot 10^{-4}$	0.97
S_2	0.11	0.11	$2 \cdot 10^{-3}$	0.95